Available online at www.sciencedirect.com
SCIENCE DIRECT®
Journal of Computational Physics 210 (2005) 554–583
JOURNAL OF COMPUTATIONAL PHYSICS
www.elsevier.com/locate/jcp

A high-order accurate hybrid scheme using a central flux scheme and a WENO scheme for compressible flowfield analysis

Dehee Kim *, Jang Hyuk Kwon

Department of Aerospace Engineering, Korea Advanced Institute of Science and Technology, 373-1 Guseong-Dong, Yuseong-Gu, Daejeon 305-701, Republic of Korea

Received 7 December 2004; received in revised form 25 April 2005; accepted 27 April 2005
Available online 5 July 2005

Abstract

A high-order accurate hybrid central-WENO scheme is proposed. The fifth order WENO scheme [G.S. Jiang, C.W. Shu, Efficient implementation of weighted ENO schemes, J. Comput. Phys. 126 (1996) 202–228] is divided into two parts, a central flux part and a numerical dissipation part, and is coupled with a central flux scheme. Two sub-schemes, the WENO scheme and the central flux scheme, are hybridized by means of a weighting function that indicates the local smoothness of the flowfields. The derived hybrid central-WENO scheme is written as a combination of the central flux scheme and the numerical dissipation of the fifth order WENO scheme, which is controlled adaptively by a weighting function. The structure of the proposed hybrid central-WENO scheme is similar to that of the YSD-type filter scheme [H.C. Yee, N.D. Sandham, M.J. Djomehri, Low-dissipative high-order shock-capturing methods using characteristic-based filters, J. Comput. Phys. 150 (1999) 199–238]. Therefore, the proposed hybrid scheme has also certain merits that the YSD-type filter scheme has. The accuracy and efficiency of the developed hybrid central-WENO scheme are investigated through numerical experiments on inviscid and viscous problems. Numerical results show that the proposed hybrid central-WENO scheme can resolve flow features extremely well.
© 2005 Elsevier Inc. All rights reserved.

Keywords: High-order scheme; Hybrid central-WENO scheme; Central flux scheme; WENO scheme

* Corresponding author. Tel.: +82 42 869 3755; fax: +82 42 869 3710.
E-mail addresses: dehee@kaist.ac.kr, dehee.kim@gmail.com (D. Kim).

0021-9991/$ - see front matter © 2005 Elsevier Inc. All rights reserved.
doi:10.1016/j.jcp.2005.04.023

1. Introduction

For unsteady flow simulations, high-order schemes are necessary for the accurate prediction of flow physics with a smaller number of grid points. High-order schemes should have low dissipative and dispersive errors for fine-scale feature capturing and shock capturing. These characteristics prevent smearing of flow features and non-physical oscillations near high gradient regions of flow variables.

Among the various numerical schemes for high-order accuracy, the ENO, WENO, and compact schemes are widely used [1–5]. The ENO and WENO schemes can resolve flow features accurately and robustly, however, they give slightly dissipative solutions. On the other hand, the compact schemes can give spectral-like resolution for linear problems, but when applying them to non-linear cases containing shocks some artificial dissipations should be added or upwinding methods should be used for numerical stability and shock capturing ability [4,6].

Recently, Yee with Sandham and Djomehri have developed a new high-order accurate filter scheme (hereafter referred to as the "YSD-type filter scheme") [7–11] that is composed of two main parts: the high-order spatial and temporal base scheme and the filter (that is, the numerical dissipation). High-order central difference and compact schemes are usually applied for the base scheme, and the dissipation parts of shock-capturing schemes such as the TVD, ENO, and WENO schemes can be utilized as the filter. The filter is for numerical stability as well as for shock and fine structure capturing. Yee et al. used the central difference scheme or the entropy splitting scheme for the base scheme and the dissipations of shock-capturing schemes with the ACM switch, and showed the capability of this system to resolve flow physics accurately with a very low cost. Post-processing of the filter gives computational efficiency because the time-consuming numerical dissipation is calculated just one time, not several times for the multistage time stepping methods. Garnier et al. [10] applied the MUSCL, ENO, and WENO dissipations to the YSD-type filter scheme and Kim and Kwon [11] presented a WENO dissipation.

A hybrid methodology that uses two sub-schemes may be another approach for high-order accuracy. Central or compact schemes can be used in smooth regions, while shock-capturing schemes such as the ENO and WENO schemes can be used in discontinuous regions with shocks. Adams and Shariff [12] have developed a hybrid compact-ENO scheme that is composed of the non-conservative compact upwind scheme and the ENO scheme. Pirozzoli [13] has proposed a hybrid compact-WENO scheme and has derived a conservative compact scheme to couple with the WENO scheme. Ren et al. [14] have improved the hybrid compact-WENO scheme proposed by Pirozzoli in several ways. They designed a continuous weighting function to prevent abrupt switching between the two sub-schemes and also proposed a characteristic-wise hybrid compact-WENO scheme that couples the Roe type, characteristic-wise compact sub-scheme and the Roe type, characteristic-wise WENO sub-scheme. Compared with the component-wise hybrid scheme suggested by Pirozzoli, Ren et al.'s characteristic-wise hybrid scheme has shown excellent improvement in resolution.

The hybrid methodology is promising in that high resolution, robustness, and computational efficiency can be achieved simultaneously.

In this paper, a hybrid central-WENO scheme is proposed. The 5th order WENO scheme (hereafter referred to as the "WENO5 scheme") is divided into two parts, a central flux part and a numerical dissipation part, and is coupled with a cell-face central flux scheme that is applied to a 6th order central difference scheme. Two sub-schemes, the WENO5 scheme and the central flux scheme, are hybridized by means of a weighting function that indicates the local smoothness of the flowfields. The derived hybrid central-WENO scheme is composed of a central flux scheme and the numerical dissipation of the WENO5 scheme, which is controlled adaptively by a weighting function. Then, the first derivative of flux at the cell center is expressed as a combination of the 6th order central difference scheme and the difference of the cell-face numerical dissipations of both sides. The adaptive control of the numerical dissipation gives improved resolution. Although this formulation is derived specifically for the

hybrid scheme, the structure of the scheme is similar to that of the YSD-type filter scheme. Therefore, the proposed hybrid central-WENO scheme has certain merits, such as the computational efficiency gained by the post-processing of the filter and the free implementation of various schemes for the linear part separately from the non-linear part.

After deriving the hybrid central-WENO scheme, we compare the performance of the WENO5 scheme and the proposed hybrid central-WENO scheme through five numerical experiments. Unsteady flowfields, such as the 1D shock/turbulence interaction [1], the advection of an isentropic vortex [7], the double Mach reflection [15], the evolving mixing layer/shock interaction [7], and the weak shock/vortex interaction [16] are simulated. The 1D shock/turbulence interaction model is used for the shock and turbulence fluctuation capturing; the advection of the Taylor vortex in an uniform flow is chosen for evaluation of the dissipative characteristics of numerical schemes; the double Mach reflection is simulated to resolve strong shocks and vortical structures; the evolving mixing-layer/shock interaction problem is chosen to investigate the accuracy of schemes for viscous flows with complicated flow structures; and the weak shock/vortex interaction is used for the prediction capability of the acoustic wave propagation. Through numerical experiments, the developed hybrid central-WENO scheme is validated. In some numerical experiments, a filter formulation that uses the 6th order Padé-type compact scheme [5] instead of the 6th order central difference scheme is applied to show the sensitivity of the solution accuracy on the scheme of the linear part.

This paper is organized as follows: In Section 2, we describe the numerical methods used for numerical simulations. Two-dimensional Navier–Stokes equations are introduced as governing equations, and the WENO5 scheme and the central flux and difference schemes are given for the upcoming hybrid central-WENO scheme. Then the hybrid central-WENO scheme is derived. The results of numerical experiments are given in Section 3. Concluding remarks are drawn in Section 4.

2. Numerical methods

2.1. Governing equations

We consider the conservative form of the two-dimensional Navier–Stokes equations as

$$\frac{\partial \mathbf{Q}}{\partial t}+\frac{\partial \mathbf{F}}{\partial x}+\frac{\partial \mathbf{G}}{\partial y}=\frac{\partial \mathbf{F}_{\mathbf{v}}}{\partial x}+\frac{\partial \mathbf{G}_{\mathbf{v}}}{\partial y} \tag{1}$$

in cartesian coordinates, where

$$\mathbf{Q}=\begin{pmatrix}\rho\\ \rho u\\ \rho v\\ \rho e\end{pmatrix},\quad \mathbf{F}=\begin{pmatrix}\rho u\\ \rho u^2+p\\ \rho uv\\ \rho uH\end{pmatrix},\quad \mathbf{G}=\begin{pmatrix}\rho v\\ \rho uv\\ \rho v^2+p\\ \rho vH\end{pmatrix}, \tag{2}$$

$$\mathbf{F}_{\mathbf{v}}=\begin{pmatrix}0\\ \tau_{xx}\\ \tau_{xy}\\ u\tau_{xx}+v\tau_{xy}+q_x\end{pmatrix},\quad \mathbf{G}_{\mathbf{v}}=\begin{pmatrix}0\\ \tau_{xy}\\ \tau_{yy}\\ u\tau_{xy}+v\tau_{yy}+q_y\end{pmatrix}, \tag{3}$$

where ρ and p are the density and pressure, u and v are the velocities of each direction. e is the total energy and H denotes the total enthalpy given by $H = e + p/\rho$. τ_{ij} and q_i mean the viscous stresses and heat fluxes, respectively.

2.2. WENO scheme

The procedure of calculating numerical fluxes at a cell face using the WENO scheme proposed by Jiang and Shu [2] can be summarized as follows:

1. Projection to the characteristic space.
2. Rusanov-type flux splitting.
3. WENO interpolation.
4. Reverse projection.

The left eigenvector matrix $\mathbf{R}^{-1}_{i+1/2}$ is used for the projection of the conservative variables and inviscid fluxes to the characteristic space,

$$\mathbf{q}_k = \mathbf{R}^{-1}_{i+1/2}\mathbf{Q}_k, \qquad \mathbf{f}_k = \mathbf{R}^{-1}_{i+1/2}\mathbf{F}_k, \quad k = i-r+1,\ldots,i+r. \tag{4}$$

For a given positive integer r, the WENO interpolation gives the $(2r-1)$th order accurate reconstructed value at the cell face $i+1/2$. The projected flux is split by flux splitting methods such as the Lax-Friedrichs-type and the Rusanov-type methods. The Lax-Friedrichs scheme and the Rusanov scheme [17] are similar in form and so they tend to be confused occasionally, but their properties are very different (see [18]). The Rusanov scheme is more accurate than the Lax-Friedrichs scheme. Therefore, the Rusanov-type flux splitting method is used, and then the flux is split as

$$f^{(l)\pm} = \frac{1}{2}(f^{(l)} \pm \lambda^{(l)}_{\max} q^{(l)}), \tag{5}$$

where the superscript l denotes each characteristic field, the signs + and − mean the positive and negative flux parts, and the scalar variables f and q are the elements of the vectors $\mathbf{f}$ and $\mathbf{q}$, respectively, and the eigenvalue $\lambda^{(l)}_{\max}$ is defined over the entire flowfield by

$$\lambda^{(l)}_{\max} = \max|\lambda^{(l)}_i|, \quad i = 1,\ldots,N, \tag{6}$$

where $\lambda^{(l)}_i$ denotes each eigenvalue of $\partial\mathbf{F}/\partial\mathbf{Q}$ in the ith node. Then, the numerical fluxes obtained by the WENO interpolation are given by

$$\hat{\mathbf{f}}_{i+1/2} = \hat{\mathbf{f}}^{+}_{i+1/2} + \hat{\mathbf{f}}^{-}_{i+1/2}, \tag{7}$$

where $\hat{\mathbf{f}}^{\pm}_{i+1/2}$ are the interpolated fluxes at the cell face $i+1/2$. Finally, the inviscid fluxes are obtained by the reverse projection as

$$\hat{\mathbf{F}}_{i+1/2} = \mathbf{R}_{i+1/2}\hat{\mathbf{f}}_{i+1/2}. \tag{8}$$

The WENO interpolation to obtain the cell-face fluxes $\hat{\mathbf{f}}^{\pm}_{i+1/2}$ is described in [2].

For brevity, the scalar notation is used for each characteristic field and the superscript l denoting each characteristic field is omitted, and a grid system is assumed uniform, $\Delta x = h$.

Let us define a general flux g that denotes the positive flux f^{+} or the negative flux f^{-}, which is split by the Rusanov-type flux splitting method as

$$\begin{pmatrix} g_{i-2} = f^{+}_{i-2} \\ g_{i-1} = f^{+}_{i-1} \\ g_i = f^{+}_i \\ g_{i+1} = f^{+}_{i+1} \\ g_{i+2} = f^{+}_{i+2} \end{pmatrix}, \quad \begin{pmatrix} g_{i-2} = f^{-}_{i+3} \\ g_{i-1} = f^{-}_{i+2} \\ g_i = f^{-}_{i+1} \\ g_{i+1} = f^{-}_i \\ g_{i+2} = f^{-}_{i-1} \end{pmatrix}, \tag{9}$$

where the left and the right equations are used to calculate the positive and negative ENO fluxes, respectively. Using Eq. (9), we can obtain three ENO fluxes with the 3rd order accuracy as:

$$\begin{aligned}
\bar{g}_0^3 &= \frac{1}{6}(2g_{i-2} - 7g_{i-1} + 11g_i),\\
\bar{g}_1^3 &= \frac{1}{6}(-g_{i-1} + 5g_i + 2g_{i+1}),\\
\bar{g}_2^3 &= \frac{1}{6}(2g_i + 5g_{i+1} - g_{i+2}),
\end{aligned} \tag{10}$$

where $\bar{g}_k^r$ $(k = 0, 1, 2,\ r = 3)$ mean the ENO fluxes. Convex sum of the three ENO fluxes gives a WENO flux $\hat{g}$, and it can be divided into two parts

$$\begin{aligned}
\hat{g}_{i+1/2} &= w_0\bar{g}_0^3 + w_1\bar{g}_1^3 + w_2\bar{g}_2^3\\
&= w_0\left(\frac{1}{3}g_{i-2} - \frac{7}{6}g_{i-1} + \frac{11}{6}g_i\right) + w_1\left(-\frac{1}{6}g_{i-1} + \frac{5}{6}g_i + \frac{1}{3}g_{i+1}\right) + w_2\left(\frac{1}{3}g_i + \frac{5}{6}g_{i+1} - \frac{1}{6}g_{i+2}\right)\\
&= w_0\left(\frac{1}{3}g_{i-2} - \frac{7}{6}g_{i-1} + \frac{11}{6}g_i\right) + w_2\left(\frac{1}{3}g_i + \frac{5}{6}g_{i+1} - \frac{1}{6}g_{i+2}\right) + (1 - w_0 - w_2)\left(-\frac{1}{6}g_{i-1} + \frac{5}{6}g_i + \frac{1}{3}g_{i+1}\right)\\
&= w_0\left(\frac{1}{3}g_{i-2} - g_{i-1} + g_i - \frac{1}{3}g_{i+1}\right) + w_2\left(\frac{1}{6}g_{i-1} - \frac{1}{2}g_i + \frac{1}{2}g_{i+1} - \frac{1}{6}g_{i+2}\right) - \frac{1}{6}g_{i-1} + \frac{5}{6}g_i + \frac{1}{3}g_{i+1}\\
&= \frac{1}{12}(-g_{i-1} + 7g_i + 7g_{i+1} - g_{i+2}) + \frac{1}{3}w_0(g_{i-2} - 3g_{i-1} + 3g_i - g_{i+1})\\
&\quad + \frac{1}{6}\left(w_2 - \frac{1}{2}\right)(g_{i-1} - 3g_i + 3g_{i+1} - g_{i+2}),
\end{aligned} \tag{11}$$

where w_0, w_1, and w_2 are weighting factors [2]. Let us define the expression $g_{i-1} - 3g_i + 3g_{i+1} - g_{i+2}$ in Eq. (11) as

$$g'''_{i+1/2} = -g_{i-1} + 3g_i - 3g_{i+1} + g_{i+2}. \tag{12}$$

In fact, Eq. (12) is the third derivative of g with the 2nd order accuracy at the cell face $i + 1/2$. Using Eqs. (5), (11), and (12), the equation for the positive WENO flux can be divided as

$$\begin{aligned}
\hat{f}^+_{i+1/2} &= w^+_{0,i+1/2}\bar{f}^{3+}_0 + w^+_{1,i+1/2}\bar{f}^{3+}_1 + w^+_{2,i+1/2}\bar{f}^{3+}_2\\
&= \frac{1}{24}(-f_{i-1} + 7f_i + 7f_{i+1} - f_{i+2}) + \frac{1}{6}w^+_{0,i+1/2}(f_{i-2} - 3f_{i-1} + 3f_i - f_{i+1})\\
&\quad + \frac{1}{12}\left(w^+_{2,i+1/2} - \frac{1}{2}\right)(f_{i-1} - 3f_i + 3f_{i+1} - f_{i+2}) + \frac{1}{2}\lambda_{\max}\hat{q}^+_{i+1/2}\\
&= \frac{1}{24}(-f_{i-1} + 7f_i + 7f_{i+1} - f_{i+2}) - \frac{1}{6}w^+_{0,i+1/2}f'''_{i-1/2} - \frac{1}{12}\left(w^+_{2,i+1/2} - \frac{1}{2}\right)f'''_{i+1/2} + \frac{1}{2}\lambda_{\max}\hat{q}^+_{i+1/2},
\end{aligned} \tag{13}$$

where $w^+_{0,i+1/2}$, $w^+_{1,i+1/2}$ and $w^+_{2,i+1/2}$ are weighting factors for the positive WENO flux, and $\hat{q}^+_{i+1/2}$ is obtained by

$$\hat{q}^+_{i+\frac{1}{2}} = \sum_{k=0}^{2} w^+_{k,i+1/2}\bar{q}^{3+}_k(q_{i+k-2}, \ldots, q_{i+k}), \tag{14}$$

where $\bar{q}_k^{3+}$ are reconstructed values at the left side of the cell face $i + 1/2$ and are given by:

$$\begin{aligned}
\bar{q}_0^{3+} &= \frac{1}{6}(2q_{i-2} - 7q_{i-1} + 11q_i),\\
\bar{q}_1^{3+} &= \frac{1}{6}(-q_{i-1} + 5q_i + 2q_{i+1}),\\
\bar{q}_2^{3+} &= \frac{1}{6}(2q_i + 5q_{i+1} - q_{i+2}).
\end{aligned} \tag{15}$$

Similarly, the equation for the negative WENO flux is derived as

$$\begin{aligned}
\hat{f}^-_{i+1/2} &= w^-_{0,i+1/2}\bar{f}^{3-}_0 + w^-_{1,i+1/2}\bar{f}^{3-}_1 + w^-_{2,i+1/2}\bar{f}^{3-}_2\\
&= \frac{1}{24}\left(-f_{i-1} + 7f_i + 7f_{i+1} - f_{i+2}\right) + \frac{1}{6}w^-_{0,i+1/2}\left(f_{i+3} - 3f_{i+2} + 3f_{i+1} - f_i\right)\\
&\quad + \frac{1}{12}\left(w^-_{2,i+1/2} - \frac{1}{2}\right)\left(f_{i+2} - 3f_{i+1} + 3f_i - f_{i-1}\right) - \frac{1}{2}\lambda_{\max}\hat{q}^-_{i+1/2}\\
&= \frac{1}{24}\left(-f_{i-1} + 7f_i + 7f_{i+1} - f_{i+2}\right) + \frac{1}{6}w^-_{0,i+1/2}f'''_{i+3/2} + \frac{1}{12}\left(w^-_{2,i+1/2} - \frac{1}{2}\right)f'''_{i+1/2} - \frac{1}{2}\lambda_{\max}\hat{q}^-_{i+1/2},
\end{aligned} \tag{16}$$

where $w^-_{0,i+1/2}$, $w^-_{1,i+1/2}$, and $w^-_{2,i+1/2}$ are also weighting factors for the negative WENO flux, and $\hat{q}^-_{i+1/2}$ is defined by

$$\hat{q}^-_{i+\frac{1}{2}} = \sum_{k=0}^{2} w^-_{k,i+1/2}\bar{q}^{3-}_k(q_{i-k+1}, \ldots, q_{i-k+3}), \tag{17}$$

where $\bar{q}_k^{3-}$ are reconstructed values at the right side of the cell face $i + 1/2$ and are given by:

$$\begin{aligned}
\bar{q}_0^{3-} &= \frac{1}{6}(2q_{i+3} - 7q_{i+2} + 11q_{i+1}),\\
\bar{q}_1^{3-} &= \frac{1}{6}(-q_{i+2} + 5q_{i+1} + 2q_i),\\
\bar{q}_2^{3-} &= \frac{1}{6}(2q_{i+1} + 5q_i - q_{i-1}),
\end{aligned} \tag{18}$$

Therefore, the WENO flux at the cell face is obtained using Eqs. (13) and (16)

$$\begin{aligned}
\hat{f}_{i+1/2} &= \hat{f}^+_{i+1/2} + \hat{f}^-_{i+1/2}\\
&= \frac{1}{12}\left(-f_{i-1} + 7f_i + 7f_{i+1} - f_{i+2}\right) + \frac{1}{6}w^+_{0,i+1/2}\left(f_{i-2} - 3f_{i-1} + 3f_i - f_{i+1}\right)\\
&\quad + \frac{1}{12}\left(w^+_{2,i+1/2} - \frac{1}{2}\right)\left(f_{i-1} - 3f_i + 3f_{i+1} - f_{i+2}\right) + \frac{1}{6}w^-_{0,i+1/2}\left(f_{i+3} - 3f_{i+2} + 3f_{i+1} - f_i\right)\\
&\quad + \frac{1}{12}\left(w^-_{2,i+1/2} - \frac{1}{2}\right)\left(f_{i+2} - 3f_{i+1} + 3f_i - f_{i-1}\right) + \frac{1}{2}\lambda_{\max}\left(\hat{q}^+_{i+1/2} - \hat{q}^-_{i+1/2}\right)\\
&= \frac{1}{12}\left(-f_{i-1} + 7f_i + 7f_{i+1} - f_{i+2}\right) - \frac{1}{6}w^+_{0,i+1/2}f'''_{i-1/2} - \frac{1}{12}\left(w^+_{2,i+1/2} - \frac{1}{2}\right)f'''_{i+1/2}\\
&\quad + \frac{1}{6}w^-_{0,i+1/2}f'''_{i+3/2} + \frac{1}{12}\left(w^-_{2,i+1/2} - \frac{1}{2}\right)f'''_{i+1/2} + \frac{1}{2}\lambda_{\max}\left(\hat{q}^+_{i+1/2} - \hat{q}^-_{i+1/2}\right).
\end{aligned} \tag{19}$$

The WENO flux at the cell face $i-1/2$ is given by

$$\begin{aligned}\hat{f}_{i-1/2} &= \hat{f}^{+}_{i-1/2} + \hat{f}^{-}_{i-1/2} \\ &= \frac{1}{12}(-f_{i-2} + 7f_{i-1} + 7f_i - f_{i+1}) - \frac{1}{6}w^{+}_{0,i-1/2}f'''_{i-3/2} - \frac{1}{12}\left(w^{+}_{2,i-1/2} - \frac{1}{2}\right)f'''_{i-1/2} \\ &\quad + \frac{1}{6}w^{-}_{0,i-1/2}f'''_{i+1/2} + \frac{1}{12}\left(w^{-}_{2,i-1/2} - \frac{1}{2}\right)f'''_{i-1/2} + \frac{1}{2}\lambda_{\max}\left(\hat{q}^{+}_{i-1/2} - \hat{q}^{-}_{i-1/2}\right). \end{aligned} \tag{20}$$

Eqs. (19) and (20) can be changed to other forms as:

$$\begin{aligned}\hat{f}_{i+1/2} &= \frac{1}{60}(f_{i-2} - 8f_{i-1} + 37f_i + 37f_{i+1} - 8f_{i+2} + f_{i+3}) - \frac{1}{6}\left(w^{+}_{0,i+1/2} - 0.1\right)f'''_{i-1/2} \\ &\quad - \frac{1}{12}\left(w^{+}_{2,i+1/2} - 0.3\right)f'''_{i+1/2} + \frac{1}{12}\left(w^{-}_{2,i+1/2} - 0.3\right)f'''_{i+1/2} + \frac{1}{6}\left(w^{-}_{0,i+1/2} - 0.1\right)f'''_{i+3/2} \\ &\quad + \frac{1}{2}\lambda_{\max}\left(\hat{q}^{+}_{i+1/2} - \hat{q}^{-}_{i+1/2}\right), \end{aligned} \tag{21}$$

$$\begin{aligned}\hat{f}_{i-1/2} &= \frac{1}{60}(f_{i-3} - 8f_{i-2} + 37f_{i-1} + 37f_i - 8f_{i+1} + f_{i+2}) - \frac{1}{6}\left(w^{+}_{0,i-1/2} - 0.1\right)f'''_{i-3/2} \\ &\quad - \frac{1}{12}\left(w^{+}_{2,i-1/2} - 0.3\right)f'''_{i-1/2} + \frac{1}{12}\left(w^{-}_{2,i-1/2} - 0.3\right)f'''_{i-1/2} + \frac{1}{6}\left(w^{-}_{0,i-1/2} - 0.1\right)f'''_{i+1/2} \\ &\quad + \frac{1}{2}\lambda_{\max}\left(\hat{q}^{+}_{i-1/2} - \hat{q}^{-}_{i-1/2}\right), \end{aligned} \tag{22}$$

where the constant 0.3 can be removed by rearranging the related terms. Eqs. (21) and (22) show that the terms related with f''' disappear in smooth regions because the weighting factors become $w_0 = 0.1$ and $w_2 = 0.3$, and then the WENO flux results in a central flux.

2.3. Central flux and difference schemes

A cell-face central flux scheme for a 4th order central difference scheme can be written as:

$$\hat{f}_{i+1/2} = \frac{1}{12}(-f_{i-1} + 7f_i + 7f_{i+1} - f_{i+2}), \tag{23}$$

$$\hat{f}_{i-1/2} = \frac{1}{12}(-f_{i-2} + 7f_{i-1} + 7f_i - f_{i+1}). \tag{24}$$

Eqs. (23) and (24) give the 4th order central difference scheme as

$$\left.\frac{\partial f}{\partial x}\right|_i = \frac{1}{h}\left(\hat{f}_{i+1/2} - \hat{f}_{i-1/2}\right) = \frac{1}{12h}(f_{i-2} - 8f_{i-1} + 8f_{i+1} - f_{i+2}) + \mathrm{O}(h^4). \tag{25}$$

Similarly, a cell-face central flux scheme for a 6th order central difference scheme is given by:

$$\hat{f}_{i+1/2} = \frac{1}{60}(f_{i-2} - 8f_{i-1} + 37f_i + 37f_{i+1} - 8f_{i+2} + f_{i+3}), \tag{26}$$

$$\hat{f}_{i-1/2} = \frac{1}{60}(f_{i-3} - 8f_{i-2} + 37f_{i-1} + 37f_i - 8f_{i+1} + f_{i+2}). \tag{27}$$

Then, the 6th order central difference scheme is written as

$$\left.\frac{\partial f}{\partial x}\right|_i = \frac{1}{h}\left(\hat{f}_{i+1/2} - \hat{f}_{i-1/2}\right) = \frac{1}{60h}\left(-f_{i-3} + 9f_{i-2} - 45f_{i-1} + 45f_{i+1} - 9f_{i+2} + f_{i+3}\right) + \mathrm{O}(h^6). \tag{28}$$

The central flux schemes for the 4th and 6th order central difference schemes are implemented to the hybrid central-WENO scheme at the boundary and interior cells, respectively. In this paper, the boundary cells mean the adjacent interior cells to the ghost cells. Using the WENO5 scheme and the central flux schemes introduced in previous and present sub-sections, a hybrid central-WENO scheme can be derived.

2.4. Hybrid central-WENO scheme

A hybrid central-WENO scheme at the cell face can be devised as:

$$\begin{aligned}\hat{f}_{i+1/2,\text{hybrid}} &= \sigma_{i+1/2}\hat{f}_{i+1/2,\text{central flux scheme}} + (1-\sigma_{i+1/2})\hat{f}_{i+1/2,\text{WENO5 scheme}},\\ \hat{f}_{i-1/2,\text{hybrid}} &= \sigma_{i-1/2}\hat{f}_{i-1/2,\text{central flux scheme}} + (1-\sigma_{i-1/2})\hat{f}_{i-1/2,\text{WENO5 scheme}},\end{aligned} \tag{29}$$

where σ is a weighting function for the hybridization of the central flux scheme and the WENO5 scheme and its range is $0 \leqslant \sigma \leqslant 1$. The WENO5 scheme has been divided previously as

$$\hat{f}_{i+1/2,\text{WENO5 scheme}} = \hat{f}_{i+1/2,\text{central flux scheme}} + \hat{f}_{i+1/2,\text{numerical dissipation}}. \tag{30}$$

Therefore, at the cell face the hybrid central-WENO scheme can be expressed as

$$\hat{f}_{i+1/2,\text{hybrid}} = \hat{f}_{i+1/2,\text{central flux scheme}} + (1-\sigma_{i+1/2})\hat{f}_{i+1/2,\text{numerical dissipation}}. \tag{31}$$

Using Eqs. (21) and (26), the hybrid central-WENO scheme is derived as

$$\begin{aligned}\hat{f}_{i+1/2,\text{hybrid}} &= \sigma_{i+1/2}\frac{1}{60}\left(f_{i-2} - 8f_{i-1} + 37f_i + 37f_{i+1} - 8f_{i+2} + f_{i+3}\right)\\ &\quad + (1-\sigma_{i+1/2})\frac{1}{60}\left(f_{i-2} - 8f_{i-1} + 37f_i + 37f_{i+1} - 8f_{i+2} + f_{i+3}\right)\\ &\quad + (1-\sigma_{i+1/2})\left\{-\frac{1}{6}\left(w^+_{0,i+1/2} - 0.1\right)f'''_{i-1/2} - \frac{1}{12}\left(w^+_{2,i+1/2} - 0.3\right)f'''_{i+1/2}\right.\\ &\quad \left. + \frac{1}{12}\left(w^-_{2,i+1/2} - 0.3\right)f'''_{i+1/2} + \frac{1}{6}\left(w^-_{0,i+1/2} - 0.1\right)f'''_{i+3/2}\right\} + (1-\sigma_{i+1/2})\frac{1}{2}\lambda_{\max}\left(\hat{q}^+_{i+1/2} - \hat{q}^-_{i+1/2}\right)\\ &= \frac{1}{60}\left(f_{i-2} - 8f_{i-1} + 37f_i + 37f_{i+1} - 8f_{i+2} + f_{i+3}\right)\\ &\quad + (1-\sigma_{i+1/2})\left\{-\frac{1}{6}\left(w^+_{0,i+1/2} - 0.1\right)f'''_{i-1/2} - \frac{1}{12}\left(w^+_{2,i+1/2} - 0.3\right)f'''_{i+1/2}\right.\\ &\quad \left. + \frac{1}{12}\left(w^-_{2,i+1/2} - 0.3\right)f'''_{i+1/2} + \frac{1}{6}\left(w^-_{0,i+1/2} - 0.1\right)f'''_{i+3/2}\right\} + \frac{1}{2}(1-\sigma_{i+1/2})\lambda_{\max}\left(\hat{q}^+_{i+1/2} - \hat{q}^-_{i+1/2}\right),\end{aligned} \tag{32}$$

Using the hybrid central-WENO scheme, the first derivative of flux at the cell center $\partial f/\partial x$ is given by

$$h\frac{\partial f}{\partial x}\Big|_i = \frac{1}{60}\left(-f_{i-3} + 9f_{i-2} - 45f_{i-1} + 45f_{i+1} - 9f_{i+2} + f_{i+3}\right) + (1-\sigma_{i+1/2})\left\{-\frac{1}{6}\left(w^+_{0,i+1/2} - 0.1\right)f'''_{i-1/2} - \frac{1}{12}\left(w^+_{2,i+1/2} - 0.3\right)f'''_{i+1/2}c + \frac{1}{12}\left(w^-_{2,i+1/2} - 0.3\right)f'''_{i+1/2} + \frac{1}{6}\left(w^-_{0,i+1/2} - 0.1\right)f'''_{i+3/2}\right\} - (1-\sigma_{i-1/2})\left\{-\frac{1}{6}\left(w^+_{0,i-1/2} - 0.1\right)f'''_{i-3/2} - \frac{1}{12}\left(w^+_{2,i-1/2} - 0.3\right)f'''_{i-1/2} + \frac{1}{12}\left(w^-_{2,i-1/2} - 0.3\right)f'''_{i-1/2} + \frac{1}{6}\left(w^-_{0,i-1/2} - 0.1\right)f'''_{i+1/2}\right\} + \frac{1}{2}(1-\sigma_{i+1/2})\lambda_{\max}\left(\hat{q}^+_{i+1/2} - \hat{q}^-_{i+1/2}\right) - \frac{1}{2}(1-\sigma_{i-1/2})\lambda_{\max}\left(\hat{q}^+_{i-1/2} - \hat{q}^-_{i-1/2}\right), \tag{33}$$

Eq. (33) is a combination of the 6th order central difference scheme and the numerical dissipation of the WENO5 scheme, which is controlled by the weighting function. This formulation can be considered as the YSD-type filter scheme, so the 6th order Padé-type compact scheme can replace the 6th order central difference scheme for the linear part. The sensitivity of the accuracy of the numerical solution on the schemes for the linear part is investigated for several numerical cases in Section 3.

At the boundary cells, to satisfy the conservation property equation (33) is changed with a combination of the 4th order central difference scheme and the numerical dissipation.

For the boundary cell $i = 1$,

$$h\frac{\partial f}{\partial x}\Big|_i = \frac{1}{12}\left(f_{i-2} - 8f_{i-1} + 8f_{i+1} - f_{i+2}\right) + (1-\sigma_{i+1/2})\left\{-\frac{1}{6}w^+_{0,i+1/2}f'''_{i-1/2} - \frac{1}{12}w^+_{2,i+1/2}f'''_{i+1/2} + \frac{1}{12}w^-_{2,i+1/2}f'''_{i+1/2} + \frac{1}{6}w^-_{0,i+1/2}f'''_{i+3/2}\right\} - \frac{1}{60}\sigma_{i+1/2}\left(f'''_{i-1/2} - f'''_{i+3/2}\right) - (1-\sigma_{i-1/2})\left\{-\frac{1}{6}w^+_{0,i-1/2}f'''_{i-3/2} - \frac{1}{12}w^+_{2,i-1/2}f'''_{i-1/2} + \frac{1}{12}w^-_{2,i-1/2}f'''_{i-1/2} + \frac{1}{6}w^-_{0,i-1/2}f'''_{i+1/2}\right\} + \frac{1}{2}(1-\sigma_{i+1/2})\lambda_{\max}\left(\hat{q}^+_{i+1/2} - \hat{q}^-_{i+1/2}\right) - \frac{1}{2}(1-\sigma_{i-1/2})\lambda_{\max}\left(\hat{q}^+_{i-1/2} - \hat{q}^-_{i-1/2}\right). \tag{34}$$

For the boundary cell $i = N$,

$$h\frac{\partial f}{\partial x}\Big|_i = \frac{1}{12}\left(f_{i-2} - 8f_{i-1} + 8f_{i+1} - f_{i+2}\right) + (1-\sigma_{i+1/2})\left\{-\frac{1}{6}w^+_{0,i+1/2}f'''_{i-1/2} - \frac{1}{12}w^+_{2,i+1/2}f'''_{i+1/2} + \frac{1}{12}w^-_{2,i+1/2}f'''_{i+1/2} + \frac{1}{6}w^-_{0,i+1/2}f'''_{i+3/2}\right\} - (1-\sigma_{i-1/2})\left\{-\frac{1}{6}w^+_{0,i-1/2}f'''_{i-3/2} - \frac{1}{12}w^+_{2,i-1/2}f'''_{i-1/2} + \frac{1}{12}w^-_{2,i-1/2}f'''_{i-1/2} + \frac{1}{6}w^-_{0,i-1/2}f'''_{i+1/2}\right\} + \frac{1}{60}\sigma_{i-1/2}\left(f'''_{i-3/2} - f'''_{i+1/2}\right) + \frac{1}{2}(1-\sigma_{i+1/2})\lambda_{\max}\left(\hat{q}^+_{i+1/2} - \hat{q}^-_{i+1/2}\right) - \frac{1}{2}(1-\sigma_{i-1/2})\lambda_{\max}\left(\hat{q}^+_{i-1/2} - \hat{q}^-_{i-1/2}\right). \tag{35}$$

2.5. Weighting functions for hybrid schemes

The weighting function plays an important role in the performance of the hybrid schemes. Several weighting functions have been proposed [7,9,12,14]. Ren et al. compared their own weighting function with the weighting function in [12] and found that their weighting function, which is a continuous function, has a more efficient switching mechanism than that by Adams and Shariff [12].

In this paper, the ACM switch and several variants of Ren et al.'s weighting function are introduced. Harten's ACM switch [7] can be simply modified to be adjusted for a weighting function as:

$$\sigma_{i+1/2} = 1 - r_{i+1/2}, \tag{36}$$

$$r_{i+1/2} = \max(\hat{r}_i, \hat{r}_{i+1}), \tag{37}$$

$$\hat{r}_{i+1/2} = \left(\frac{\|\alpha_{i+1/2}| - |\alpha_{i-1/2}\|}{|\alpha_{i+1/2}| + |\alpha_{i-1/2}| + \epsilon_2} \right)^p, \tag{38}$$

where $\alpha_{i+1/2} = q_{i+1} - q_i$ and ϵ_2 is set to 10^{-6}. The difference of projected physical flux on the characteristic space Δf can take the place of the difference of characteristic variable α. Generally, there is not a distinguishable difference between two cases.

The weighting function proposed by Ren et al. is written as:

$$\sigma_{i+1/2} = \min\left(1, \frac{r_{i+1/2}}{r_c}\right), \tag{39}$$

$$r_{i+1/2} = \min(r_i, r_{i+1}), \tag{40}$$

where r_c is a threshold value that is usually problem-dependent and r_i is defined by

$$r_i = \frac{|2\Delta f_{i+1/2}\Delta f_{i-1/2}| + \epsilon_3}{(\Delta f_{i+1/2})^2 + (\Delta f_{i-1/2})^2 + \epsilon_3}, \tag{41}$$

where

$$\Delta f_{i+1/2} = f_{i+1} - f_i, \quad \epsilon_3 = \frac{0.9 r_c}{1 - 0.9 r_c}\xi^2, \tag{42}$$

where ϵ_3 prevents division by zero and can be controlled subtly by the threshold values r_c and ξ. The weighting function σ is calculated on each characteristic field. This weighting function can be modified in two ways. Firstly, r_i can be modified slightly as

$$r_i = \frac{|2\Delta f_{i+1/2}\Delta f_{i-1/2}|}{(\Delta f_{i+1/2})^2 + (\Delta f_{i-1/2})^2 + \epsilon_4}, \tag{43}$$

where

$$\epsilon_4 = \frac{0.9 r_c}{1 - 0.9 r_c}\xi. \tag{44}$$

This equation gives enhanced robustness for the proposed hybrid scheme. Another option is to replace the original $r_{i+1/2}$ by

$$r_{i+1/2} = \min(r_{i-1}, r_i, r_{i+1}, r_{i+2}). \tag{45}$$

Eq. (45) shows a rather robust behavior but gives a little dissipative solution. Ren et al.'s original weighting function is named "type A", and its two variants, Eqs. (43) and (45), are named "type B" and "type C", respectively. Throughout all the flow simulations, "type B" is used as a weighting function, and its performance is compared to the performances of several other weighting functions on the 1D shock/turbulence interaction problem in the numerical experiments section. The threshold value ξ is set to 10^{-3} for all cases, except following the scalar advection equation case, and only r_c is chosen problem-dependently. Here, the sensitivity of the solution accuracy on r_c is investigated for

a scalar advection problem with a complicated initial condition. Section 8.1 in [2] illustrates the problem in detail, so the equations and initial conditions are omitted. The problem contains a narrow combination of Gaussians, a square wave, a sharp triangle wave, and a half ellipse. The computation domain is $-1 \leqslant x \leqslant 1$ and the boundaries of both sides are periodic. We compute up to $t = 20$ and 100 with 201 nodes. For this problem, the Roe-type WENO scheme is used instead of the WENO scheme that uses flux splitting and ξ for the hybrid central-WENO scheme is set to 0.1. Solutions using the WENO5 scheme and the hybrid central-WENO scheme are shown in Fig. 1. While r_c values less than 0.4 give very accurate results, r_c values greater than 0.5 give slightly dissipative solutions. Computations with r_c under 0.05 appear to be unstable. Generally, an r_c less than a certain value no longer yields an improved solution and actually results in unstable computation. At $t = 100$, the hybrid central-WENO scheme gives much better result compared with the WENO5 scheme.

2.6. Viscous fluxes

The 6th order central difference schemes for viscous fluxes are used to obtain the overall high-order accuracy for viscous problems. For flow variables and dependent variables, the 6th order interpolation and differencing methods should be implemented. Deng and Mao [19] used the 4th order accurate methods, and those methods have been extended to the 6th order accuracy in this paper. In following equations, 1 and N mean the first and last cells, 1/2 and $N + 1/2$ denote the boundaries, 0 and $N + 1$ describe the ghost cells.

The first derivatives at the cell faces are written as:

$$
\begin{aligned}
u'_{1/2} &= \frac{1}{24h}(-22u_0 + 17u_1 + 9u_2 - 5u_3 + u_4),\\
u'_{3/2} &= \frac{27}{24h}(u_2 - u_1) - \frac{1}{24h}(u_3 - u_0),\\
u'_{i+1/2} &= \frac{2250}{1920h}(u_{i+1} - u_i) - \frac{125}{1920h}(u_{i+2} - u_{i-1}) + \frac{9}{1920h}(u_{i+3} - u_{i-2}),\\
u'_{N-1/2} &= \frac{27}{24h}(u_N - u_{N-1}) - \frac{1}{24h}(u_{N+1} - u_{N-2}),\\
u'_{N+1/2} &= -\frac{1}{24h}(-22u_{N+1} + 17u_N + 9u_{N-1} - 5u_{N-2} + u_{N-3}),
\end{aligned}
\tag{46}
$$

where u is a temporary variable for expressions and does not mean the velocity.

The first derivatives at the cell centers are given by:

$$
\begin{aligned}
u'_1 &= \frac{1}{12h}(-3u_0 - 10u_1 + 18u_2 - 6u_3 + u_4),\\
u'_2 &= \frac{8}{12h}(u_3 - u_1) - \frac{1}{12h}(u_4 - u_0),\\
u'_i &= \frac{45}{60h}(u_{i+1} - u_{i-1}) - \frac{9}{60h}(u_{i+2} - u_{i-2}) + \frac{1}{60h}(u_{i+3} - u_{i-3}),\\
u'_{N-1} &= \frac{8}{12h}(u_N - u_{N-2}) - \frac{1}{12h}(u_{N+1} - u_{N-3}),\\
u'_N &= -\frac{1}{12h}(-3u_{N+1} - 10u_N + 18u_{N-1} - 6u_{N-2} + u_{N-3}).
\end{aligned}
\tag{47}
$$

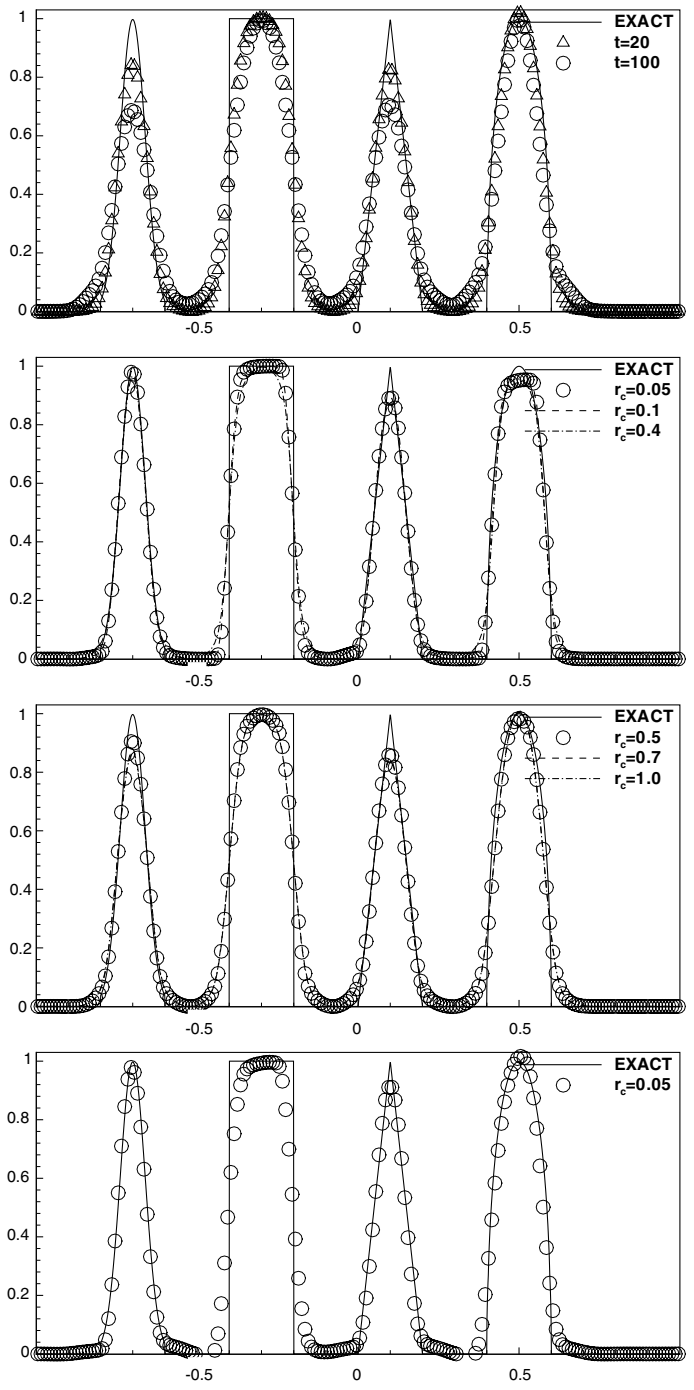

Fig. 1. The sensitivity of the solution accuracy on the threshold value r_c for a linear advection equation: the WENO5 scheme at $t = 20$ and 100 (1st), the hybrid central-WENO scheme at $t = 20$ with $r_c = 0.05$, 0.1, and 0.4 (2nd), the hybrid central-WENO scheme at $t = 20$ with $r_c = 0.5$, 0.7, and 1.0 (3rd), the hybrid central-WENO scheme at $t = 100$ with $r_c = 0.05$ (4th).

The interpolations at the cell faces can be expressed as:

$$\begin{aligned}
u_{1/2} &= \frac{1}{16}(5u_0 + 15u_1 - 5u_2 + u_3),\\
u_{3/2} &= \frac{9}{16}(u_2 + u_1) - \frac{1}{16}(u_3 + u_0),\\
u_{i+1/2} &= \frac{150}{256}(u_{i+1} + u_i) - \frac{25}{256}(u_{i+2} + u_{i-1}) + \frac{3}{256}(u_{i+3} + u_{i-2}),\\
u_{N-1/2} &= \frac{9}{16}(u_N + u_{N-1}) - \frac{1}{16}(u_{N+1} + u_{N-2}),\\
u_{N+1/2} &= \frac{1}{16}(5u_{N+1} + 15u_N - 5u_{N-1} + u_{N-2}).
\end{aligned} \tag{48}$$

Then, the viscous residuals are obtained by

$$\left.\frac{\partial \mathbf{F}_\mathbf{v}}{\partial x}\right|_i = \frac{75}{64h}\left(\hat{\mathbf{F}}_{\mathbf{v},i+1/2} - \hat{\mathbf{F}}_{\mathbf{v},i-1/2}\right) - \frac{25}{384h}\left(\hat{\mathbf{F}}_{\mathbf{v},i+3/2} - \hat{\mathbf{F}}_{\mathbf{v},i-3/2}\right) + \frac{3}{640h}\left(\hat{\mathbf{F}}_{\mathbf{v},i+5/2} - \hat{\mathbf{F}}_{\mathbf{v},i-5/2}\right), \tag{49}$$

where $\hat{\mathbf{F}}_{\mathbf{v},i+1/2}$ denote the numerical viscous fluxes at the cell face calculated by the above equations.

2.7. Time marching methods

For the accurate time integration, the multistage time stepping methods are usually applied for the high-order schemes. The 4th order accurate Runge–Kutta method or Shu's 3rd order TVD time stepping method can be used. In this paper, the 4th order Runge–Kutta method is applied for the unsteady time integrations.

The classical Runge–Kutta method is written as:

$$\begin{aligned}
\mathbf{Q}^{(1)} &= \mathbf{Q}^n + \frac{1}{2}\Delta t\mathbf{L}(\mathbf{Q}^n),\\
\mathbf{Q}^{(2)} &= \mathbf{Q}^n + \frac{1}{2}\Delta t\mathbf{L}(\mathbf{Q}^{(1)}),\\
\mathbf{Q}^{(3)} &= \mathbf{Q}^n + \Delta t\mathbf{L}(\mathbf{Q}^{(2)}),\\
\mathbf{Q}^{n+1} &= \mathbf{Q}^n + \frac{1}{6}\Delta t\left[\mathbf{L}(\mathbf{Q}^n) + 2\mathbf{L}(\mathbf{Q}^{(1)}) + 2\mathbf{L}(\mathbf{Q}^{(2)}) + \mathbf{L}(\mathbf{Q}^{(3)})\right],
\end{aligned} \tag{50}$$

where $\mathbf{L}$ denotes a residual operator.

Another time marching strategy is to calculate only the central flux at four stages and to post process the numerical dissipation after four stages [7]. This is efficient because the time-consuming numerical dissipation term is calculated only once at every time step; only the central flux is calculated each stage and the numerical dissipation is added just at the end. This approach is very time efficient but is limited when dealing with challenging problems, such as flows that have strong shocks, so only the classical 4th order Runge–Kutta method is implemented.

2.8. Stability analyses

For a linear advection equation as

$$u_t + au_x = 0, \quad a > 0, \tag{51}$$

the von Neumann stability analysis is carried out. Theories on the Fourier mode are well written in [20], and a simplified version is available in [13]. It is assumed that the spatial discretization using the WENO5 scheme and the hybrid central-WENO scheme is performed in smooth regions. The spatial discretization in the Fourier mode is expressed as the *transfer function* $Z(\hat{k})$ in [13]. When $Z(\hat{k})$ is given, the *amplification*

factor $A(\hat{k})$ can be calculated. The linear equation is fully discretized with spatial discretization methods and the 4th order Runge–Kutta method, then $A(\hat{k})$ is written as

$$A(\hat{k}) = \left[1 + \mathrm{i}\sigma Z + \frac{1}{2}(\mathrm{i}\sigma Z)^2 + \frac{1}{6}(\mathrm{i}\sigma Z)^3 + \frac{1}{24}(\mathrm{i}\sigma Z)^4\right], \tag{52}$$

where $\hat{k}$ is a scaled wavenumber. $Z(\hat{k})$ for the WENO5 scheme is given by

$$Z(\hat{k}) = -\frac{1}{30}\sin 0.5\hat{k}\frac{\left[47 + 14\cos\hat{k} - \cos 2\hat{k} + \mathrm{i}(40\sin\hat{k} - 5\sin 2\hat{k})\right]}{\cos 0.5\hat{k} + \mathrm{i}\sin 0.5\hat{k}} \tag{53}$$

and for the hybrid central-WENO scheme is written as

$$Z(\hat{k}) = -\frac{1}{30}\sin 0.5\hat{k}\frac{\left[37 + 29\cos\hat{k} - 7\cos 2\hat{k} + \cos 3\hat{k} + \mathrm{i}(45\sin\hat{k} - 9\sin 2\hat{k} + \sin 3\hat{k})\right]}{\cos 0.5\hat{k} + \mathrm{i}\sin 0.5\hat{k}}. \tag{54}$$

Using Eqs. (52)–(54), $A(\hat{k})$ is plotted in polar coordinates as Fig. 2. The stable condition $|A| \leqslant 1$ gives following stable ranges of the Courant number $\sigma = a\Delta t/\Delta x$

$$\sigma_{\mathrm{WENO5}} \leqslant 1.732, \quad \sigma_{\mathrm{hybrid}} \leqslant 1.783. \tag{55}$$

3. Numerical experiments

Three inviscid and two viscous flow problems are chosen for validation of the proposed hybrid central-WENO scheme. Several weighting functions are applied to the 1D shock/turbulence interaction problem in order to compare their performances, and only "type B" is used for the other cases.

3.1. Interaction of a moving shock with a density wave

We applied the developed hybrid central-WENO scheme to the Shu and Osher's 1D shock/turbulence interaction model problem [1]. This problem simulates the interaction between a moving Mach 3 shock wave and a fluctuating density sine wave [21]. The initial flow conditions are given by:

$$\begin{aligned} &\rho_{\mathrm{L}} = 3.857143, \quad \rho_{\mathrm{R}} = 1 + 0.2\sin(5x), \\ &u_{\mathrm{L}} = 2.629369, \quad u_{\mathrm{R}} = 0, \\ &p_{\mathrm{L}} = 10.33333, \quad p_{\mathrm{R}} = 1, \end{aligned} \tag{56}$$

where the left and right sides of $x = -4$ are denoted as subscripts L and R, respectively. The flowfield, $-5 \leqslant x \leqslant 5$, is covered with 201 nodes and the CFL number is set to 0.5. We compute up to $t = 1.8$. The reference data were obtained using the WENO5 scheme with 1601 grid points and it is assumed as the exact solution. The solutions using the WENO5 scheme, Pirozzoli's component-wise hybrid compact-WENO scheme, Ren et al.'s characteristic-wise hybrid compact-WENO scheme, and the present hybrid central-WENO scheme are shown in Fig. 3. All solutions using the hybrid schemes were computed with 201 grid points and results using the WENO5 scheme were obtained with 201 and 401 grid points. r_{c} was set to 0.3 for Ren et al.'s hybrid scheme and the present hybrid scheme, but it was set to 1.0 for Pirozzoli's hybrid scheme to obtain stable solution. As seen in Fig. 3, the WENO5 scheme is too dissipative to resolve all the fluctuations with 201 points, but can capture flow features with 401 points. Pirozzoli's hybrid scheme is more accurate than the WENO5 scheme, but Ren et al.'s hybrid scheme and the present hybrid scheme both outperform all the other schemes implemented in this case.

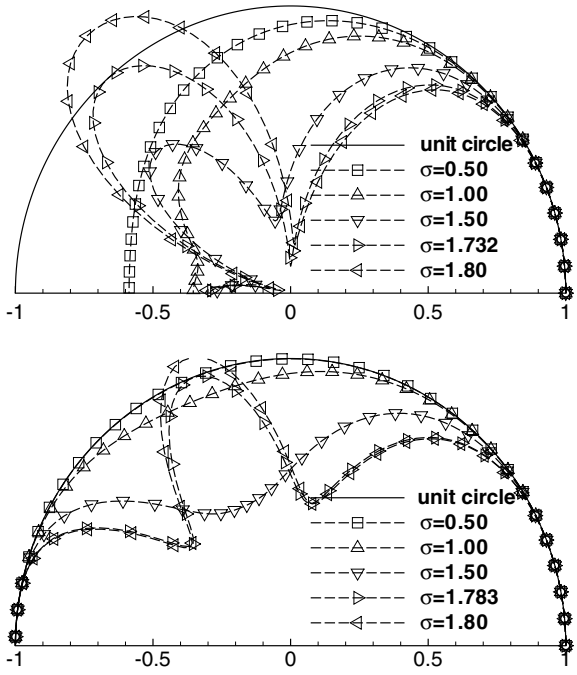

Fig. 2. Stability analyses: the WENO5 scheme (top), the hybrid central-WENO scheme (bottom).

Furthermore, although Ren et al.'s hybrid scheme can resolve the contact discontinuity more accurately because of its implementation of the Roe-type WENO scheme, the proposed hybrid scheme can achieve comparable resolution. It is found that the resolution using Ren et al.'s scheme and the present hybrid scheme is similar to that using the WENO5 scheme with 401 points. The ACM switch and the variants of Ren et al.'s original weighting function were investigated and the performances are shown in Fig. 4. The ACM switch is not as efficient as the family of Ren et al.'s weighting function. "Type A" and "type B" show similar performances, but "type C" is not quite as good as the other two types. The filter formulation that uses the 6th order Padé-type compact scheme with a WENO filter ("WF") was applied to test the accuracy. As the results in Fig. 5 show, the filter formulation does not give an improved resolution. This poor resolution is caused by the lack of harmony between the compact scheme and the WENO filter. Figs. 6 and 7 show the influence of the threshold value r_c for the hybrid central-WENO scheme with 201 and 401 grid points. For a coarse grid system the influence of r_c is apparent, while for a fine grid system varying r_c does not show a meaningful difference between numerical solutions. Generally as r_c increases, the WENO5 scheme becomes more dominant over the flowfield and the hybrid central-WENO scheme gives more dissipative solutions. The computational efficiency is found in Table 1. All data are normalized by the overall computing time of simulation using the 2nd order upwind TVD scheme. It is necessary to compare the overall computing time instead of the flux function computing time since the efficiency of hybrid schemes should be estimated over the entire flowfield. Ren et al.'s hybrid scheme takes over twice as long as the other hybrid schemes and the WENO5 scheme. The slowness of the scheme is due to the inversion of the block tridiagonal matrix related with the characteristic-wise compact scheme. Considering the computing time and the resolution power together, the proposed hybrid central-WENO scheme shows the best performance among the schemes implemented.

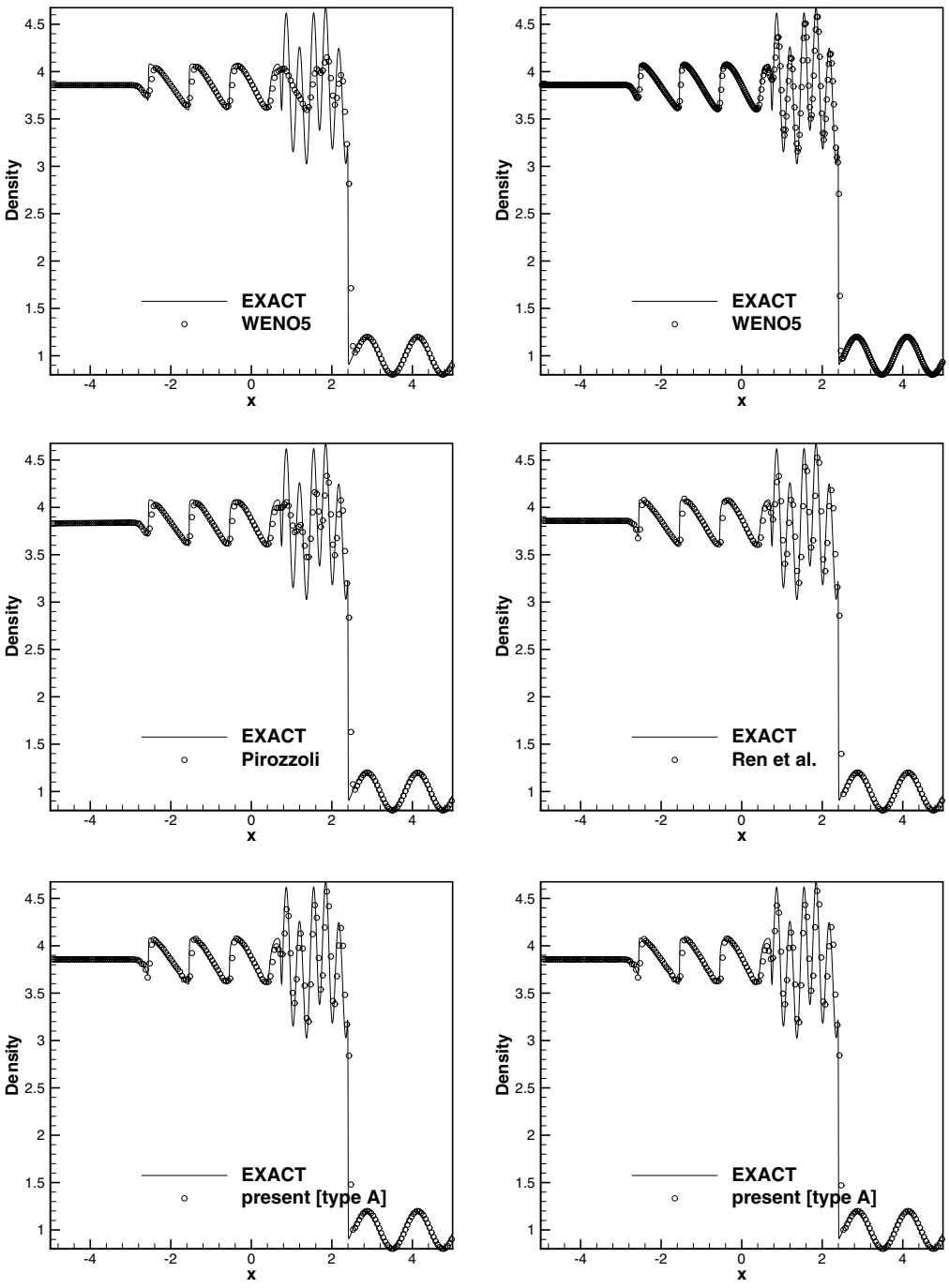

Fig. 3. Density distributions of the 1D shock/turbulence interaction at $t = 1.8$: the WENO5 scheme with 201 nodes (top left) and 401 nodes (top right), Pirozzoli's hybrid scheme [$r_c = 1.0$] (middle left), Ren et al.'s hybrid scheme [$r_c = 0.3$] (middle right), the present hybrid central-WENO scheme with type A [$r_c = 0.3$] (bottom left) and [$r_c = 0.26$] (bottom right).

3.2. Advection of an isentropic vortex

This problem was chosen in Yee et al. [7] to assess the performance of numerical schemes. An isentropic vortex convects in an inviscid free stream. This test validates that the schemes can give low-dissipative solutions for long-time integration. The computations are performed on the flow domain of $0 \leqslant x \leqslant 10$, $-5 \leqslant y \leqslant 5$. The isentropic vortex is added to the mean flowfield and the initial mean flow and disturbed values are given by:

$$
\begin{aligned}
&u_\infty = 1, \quad v_\infty = 0, \quad p_\infty = \rho_\infty = 1, \\
&(\delta u, \delta v) = \frac{\beta}{2\pi} \mathrm{e}^{(1-r^2)/2}(-\bar{y}, \bar{x}), \\
&\delta T = -\frac{(\gamma-1)\beta^2}{8\gamma\pi^2} \mathrm{e}^{(1-r^2)}, \\
&r^2 = \bar{x}^2 + \bar{y}^2, \\
&\bar{x} = x - x_{\mathrm{vc}}, \quad \bar{y} = y - y_{\mathrm{vc}},
\end{aligned}
\tag{57}
$$

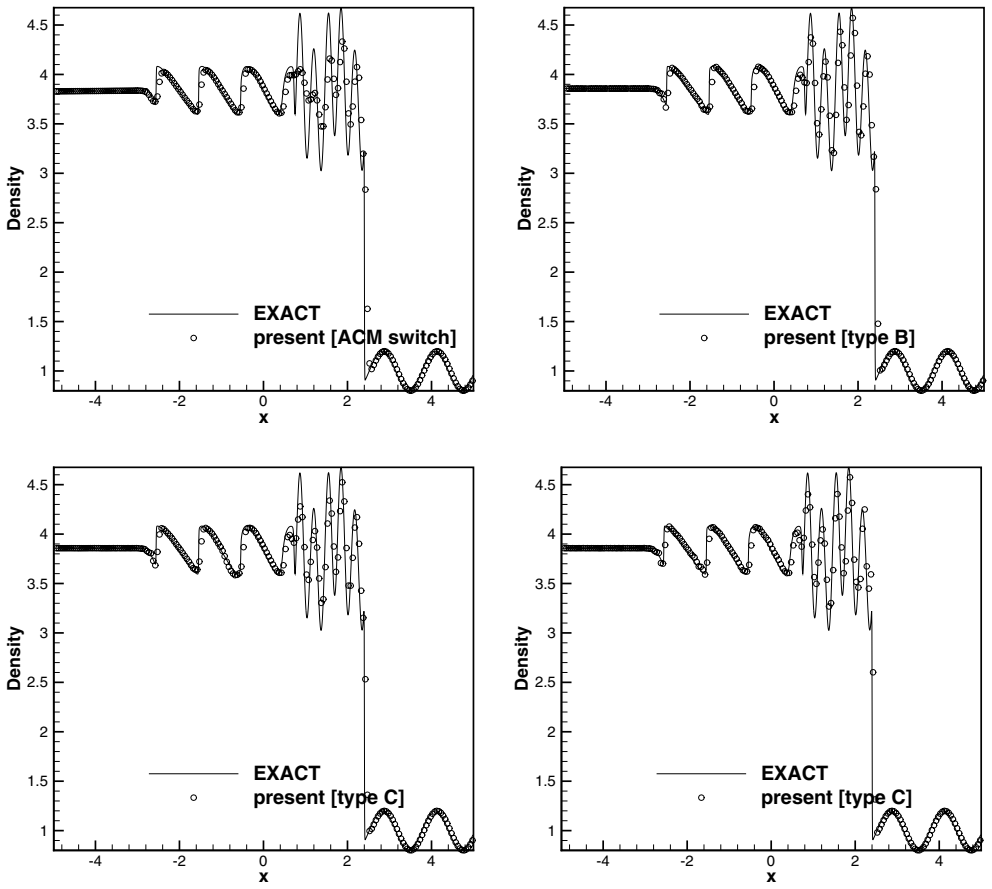

Fig. 4. Density distributions of the 1D shock/turbulence interaction at $t = 1.8$ using the present hybrid central-WENO scheme with several weighting functions: ACM switch (top left), type B [$r_c = 0.3$] (top right), type C [$r_c = 0.3$] (bottom left), type C [$r_c = 0.17$] (bottom right).

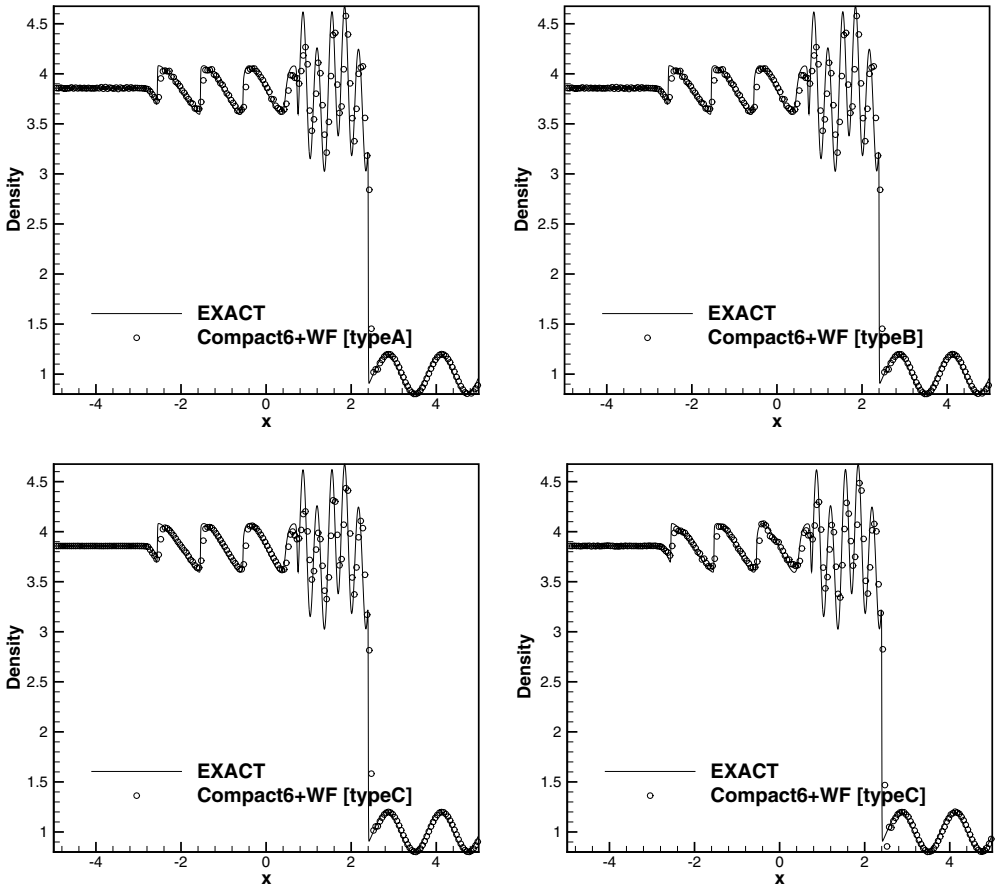

Fig. 5. Comparison of density distributions of the 1D shock/turbulence interaction at $t = 1.8$ using the filter formulation (compact6 + WENO filter) with several weighting functions: type A [$r_c = 0.3$] (top left), type B [$r_c = 0.3$] (top right), type C [$r_c = 0.3$] (bottom left), type C [$r_c = 0.15$] (bottom right), 201 nodes.

where β is the vortex intensity set to 5 and (x_{vc},y_{vc}) are the coordinates of the center of initial vortex: $(x_{vc},y_{vc}) = (5,0)$. Periodic boundary conditions in both directions are implemented. The vortex convects to the right with the free stream and is placed at the initial location every non-dimensional time interval $\Delta t = 10$. When the time goes by $t = 1000$, the initial vortex passes through the initial vortex center 100 times. Since the flowfield is inviscid, low-dissipative characteristics of each scheme can be found by comparing the vortex shape or the density profile along the center line ($y = 0$) with the initial data. Figs. 8 and 9 show density contours using the WENO5 scheme and the hybrid central-WENO scheme, respectively. An 81×80 uniform grid system was used and the time step size was set to 0.04. r_c was set to 0.1 for the hybrid central-WENO scheme. In Fig. 8, the vortex begins to smear after $t = 500$ due to excessive numerical dissipation of the WENO5 scheme. As seen in Fig. 9, the hybrid central-WENO scheme can retain the vortex shape well. Fig. 10 shows a comparison of density distributions along the center line using the WENO5 scheme, the hybrid central-WENO scheme, and the filter formulation with the compact scheme for the linear part. At $t = 1000$, the WENO5 scheme gives a smeared solution, while the hybrid central-WENO scheme shows an accurate resolution. The difference between the filter formulation and the hybrid

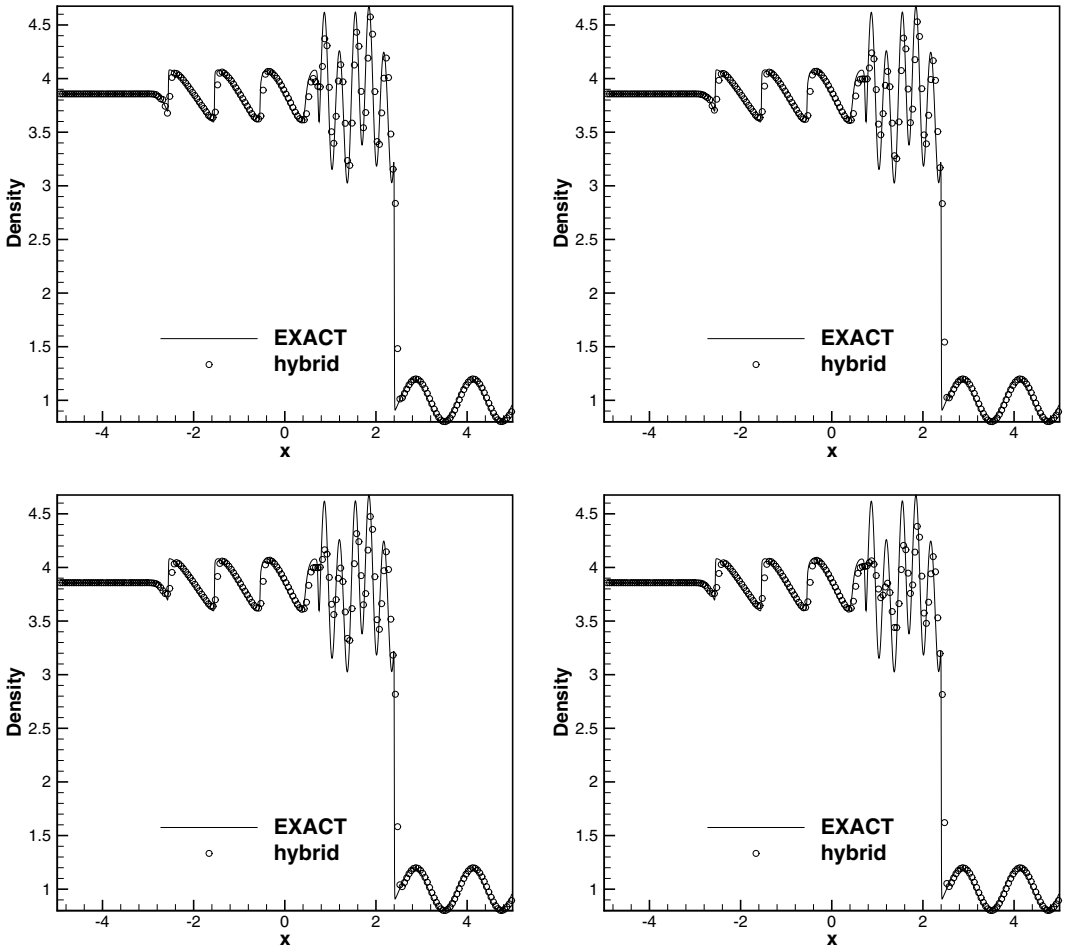

Fig. 6. Influence of the threshold value r_c, density distributions of the 1D shock/turbulence interaction at $t = 1.8$ using the present hybrid central-WENO scheme [type B] with 201 nodes: $r_c = 0.3$ (top left), $r_c = 0.5$ (top right), $r_c = 0.7$ (bottom left), $r_c = 1.0$ (bottom right).

formulation is indistinguishable. The influence of the threshold value r_c is also found. Although the increased r_c gives a dissipative solution, it is only very slightly dissipative. Fig. 11 illustrates the results using a smaller number of grid points, 41×40. Although the vortex is smeared as time passes, the hybrid central-WENO scheme gives less dissipative solutions than the WENO5 scheme. The effect of the time step size has been investigated using various time step sizes, $\Delta t = 0.01$, 0.02, and 0.04. Because the influence of the time step size on the solution accuracy was negligible for both schemes in this problem, the results are not shown here.

3.2.1. Convergence test

For a convergence test, the advection of an isentropic vortex with an incline of 45° to the $y = 0$ line is simulated using various grid sizes: 25×25, 50×50, 75×75, and 100×100. The initial conditions differ from Eq. (57) only in $v_\infty = 1$. The vortex relocates to the initial position at a time interval of 10. The data after 1

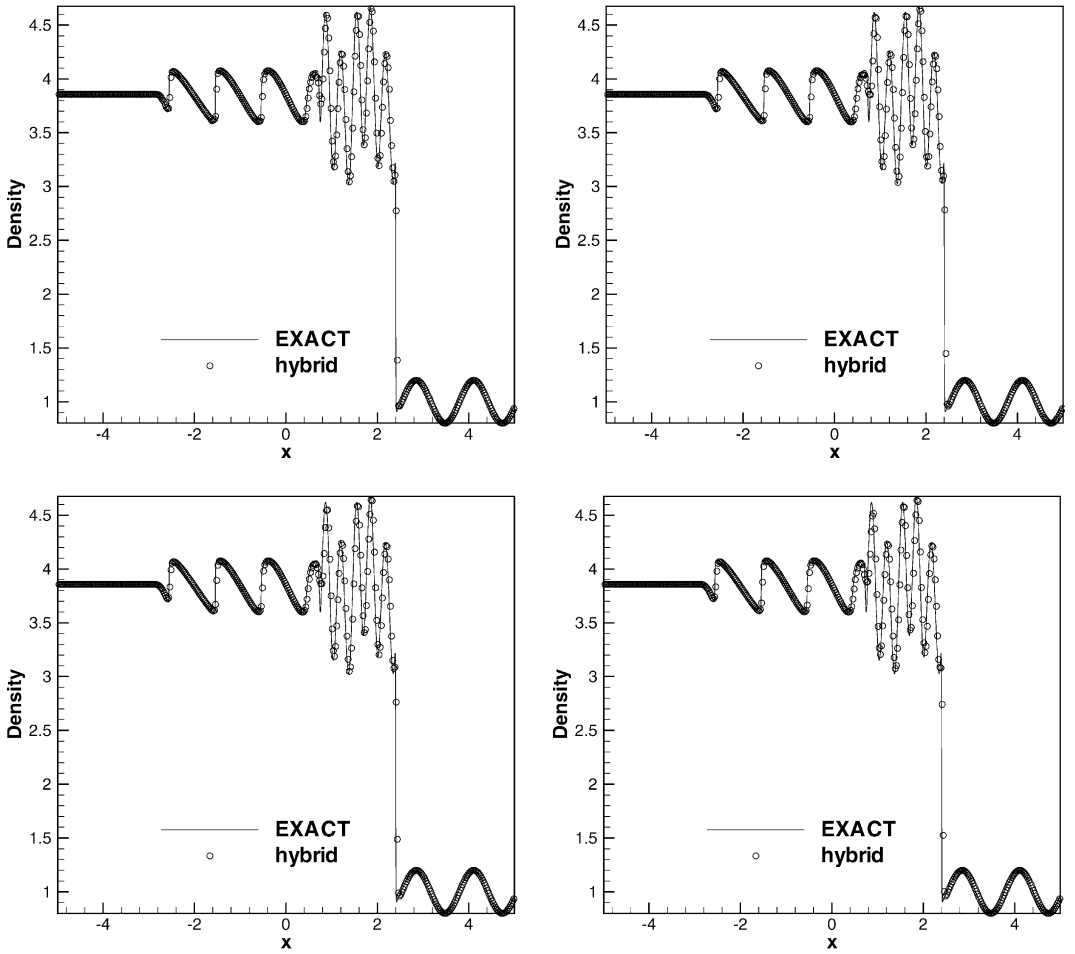

Fig. 7. Influence of the threshold value r_c, density distributions of the 1D shock/turbulence interaction at $t = 1.8$ using the hybrid central-WENO scheme, 401 nodes: $r_c = 0.3$ (top left), $r_c = 0.5$ (top right), $r_c = 0.7$ (bottom left), $r_c = 1.0$ (bottom right).

Table 1
Computational efficiency

Scheme	Computing time
TVD	1.00
WENO5	2.27
Pirozzoli	2.73
Ren et al.	5.86
Present [type A]	2.09
Present [type B]	2.15
Present [type C]	2.55

period are shown in Table 2. The hybrid central-WENO scheme shows L_1 and L_∞ orders similar to those of the WENO5 scheme, but L_1 and L_∞ errors of the hybrid central-WENO scheme are much lower than those of the WENO5 scheme.

3.3. Double Mach reflection of a strong shock

This is a well known test case for high resolution schemes [15]. Results of using the WENO5 scheme with various grid sizes are found in [22]. The problem involves a Mach 10 shock in air ($\gamma = 1.4$) which makes an angle of 60° with a reflecting wall. The computational domain of this problem is a tunnel 4 units long and 1 unit high, starting at $(x,y) = (0,0)$. Initially, the shock extends from the point $x = 1/6$ at the bottom of problem domain, to the top of problem domain at $y = 1$. The undisturbed air ahead of the shock has a density of 1.4 and a pressure of 1. The reflecting wall lies along the bottom of problem domain, beginning at $x = 1/6$. Post-shock conditions are assigned at the left-hand boundaries of the shock. Outflow boundary conditions are applied at the right end of domain $x = 4$. The values on the top boundary are set to describe the exact motion of a Mach 10 shock. All data are obtained at $t = 0.2$ and the CFL number is set to 0.5. Fig. 12 shows density contours using the WENO5 scheme and the hybrid central-WENO scheme. The first figure

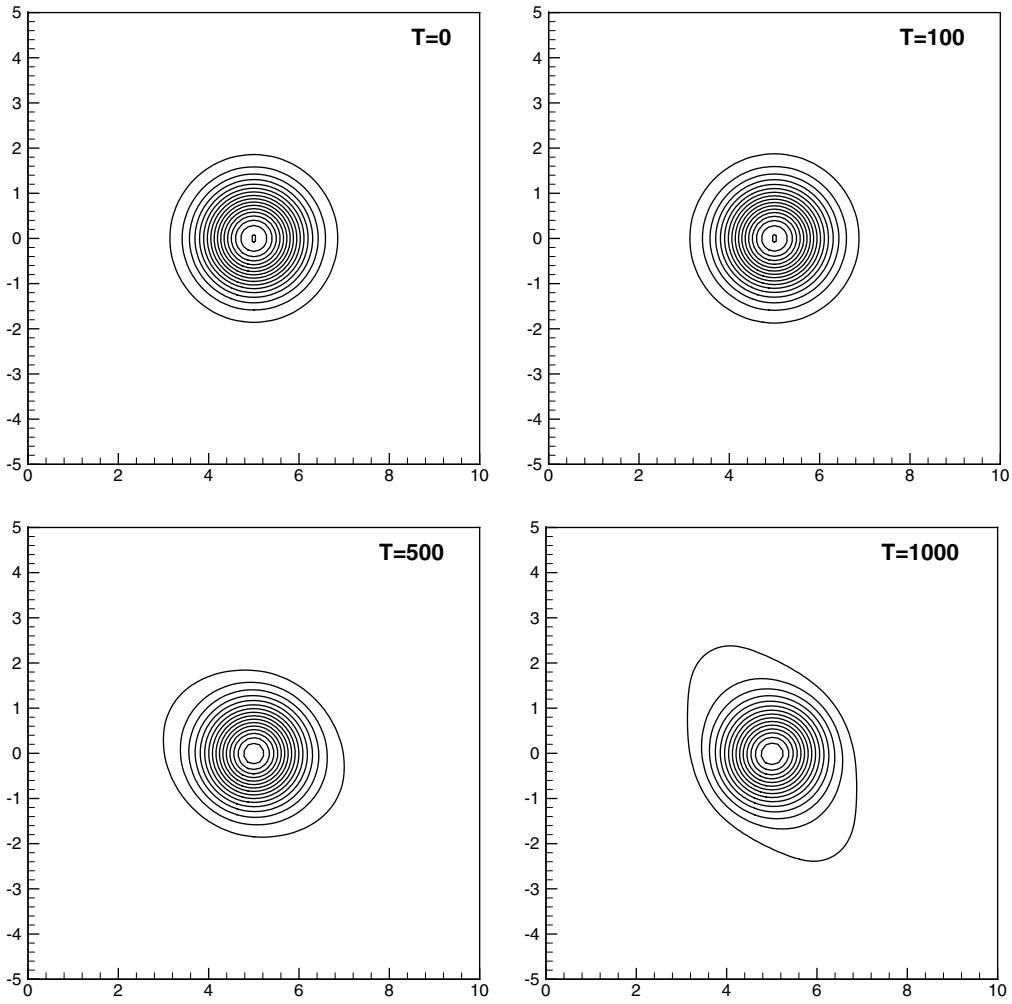

Fig. 8. Density contours of the convecting vortex at $t = 0$, 100, 500, and 1000 using the WENO5 scheme with a 81×80 grid system: equally spaced 17 contours (min = 0.5, max = 0.98).

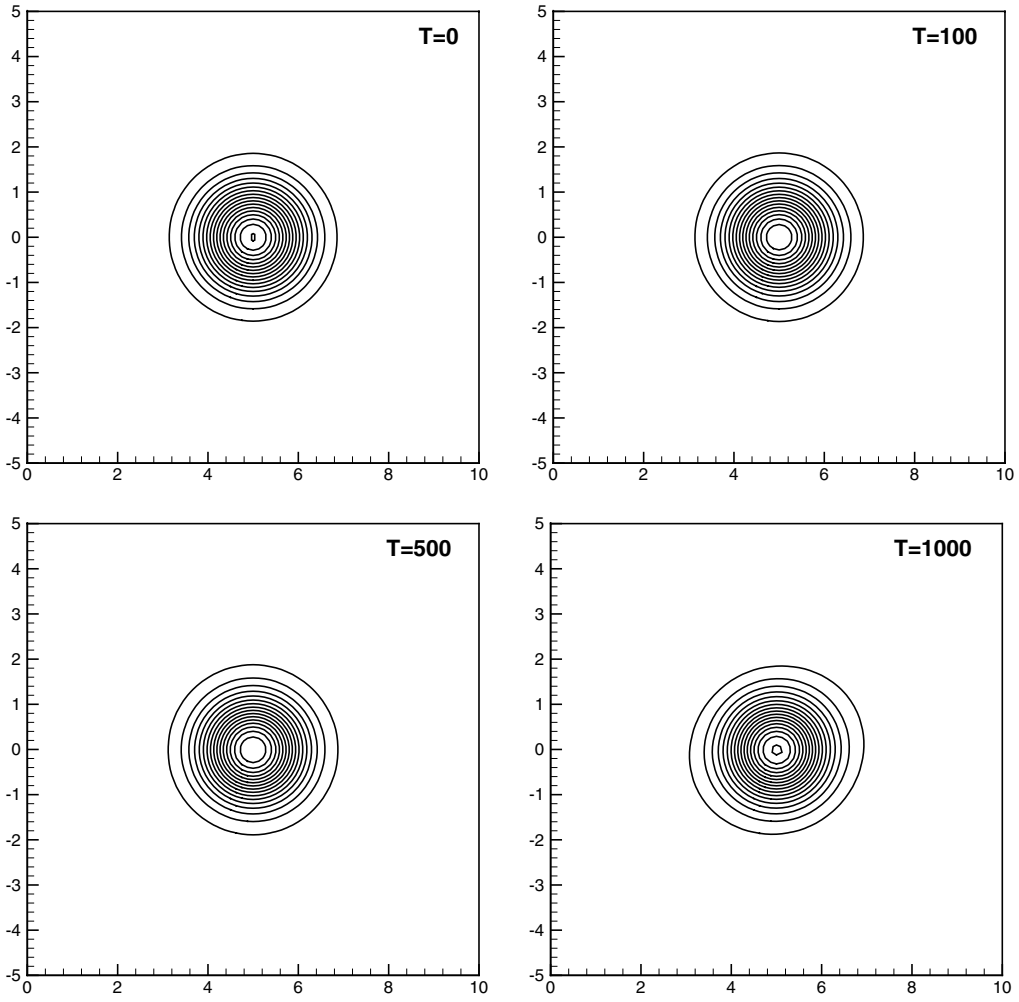

Fig. 9. Density contours of the convecting vortex at $t = 0$, 100, 500, and 1000 using the hybrid central-WENO scheme [$r_c = 0.1$] with a 81×80 grid system: equally spaced 17 contours (min = 0.5, max = 0.98).

shows the result of using the WENO5 scheme with a 961×241 uniform grid system. The second, third, and fourth figures show the results of using the hybrid central-WENO scheme with 481×121, 721×201, and 961×241 uniform grid systems, respectively. $r_c = 0.3$ was given for all the simulations using the proposed hybrid central-WENO scheme. The complicated flow features in the "blow-up" region around the double Mach stems are resolved well by the hybrid central-WENO scheme. The hybrid central-WENO scheme can capture the vortical flow structures along the slip line very well. The hybrid central-WENO scheme with $r_c = 0.2$ can give a solution that is slightly better than that with $r_c = 0.3$, but the result is not displayed to save the space. The close-up view around the "blow-up" region is shown in Fig. 13. The hybrid central-WENO scheme can roughly capture the vortical structures just with a 481×121 grid system. The carbuncle phenomenon related with the Roe-type scheme near the stronger Mach stem can be avoided even without a special entropy treatment [3]. The filter formulation with the compact scheme is unstable for this type of strong shocks because completely switching to the WENO5 scheme around high-gradient regions of

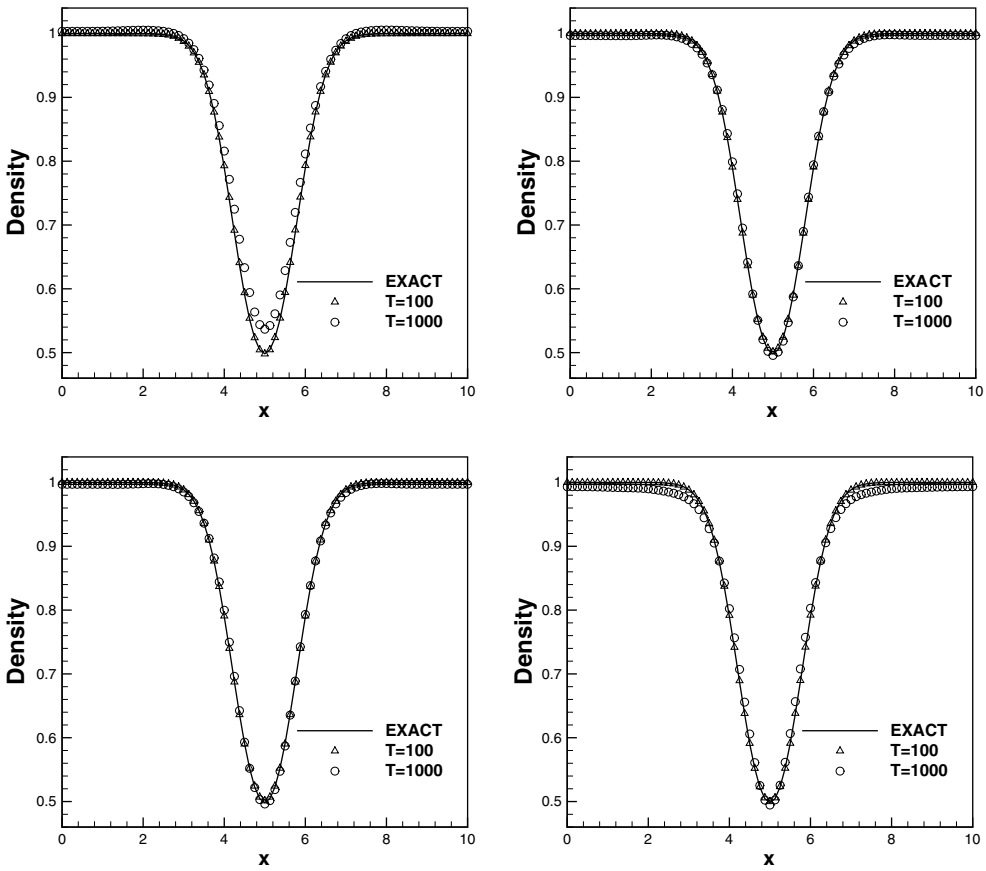

Fig. 10. Density distributions of the convecting vortex along the center line at $t = 100$ and 1000: the WENO5 scheme (top left), the hybrid central-WENO scheme [$r_c = 0.1$] (top right), the filter formulation (compact6 + WENO filter) [$r_c = 0.1$] (bottom left), the hybrid central-WENO scheme [$r_c = 0.3$] (bottom right), a 81×80 grid system.

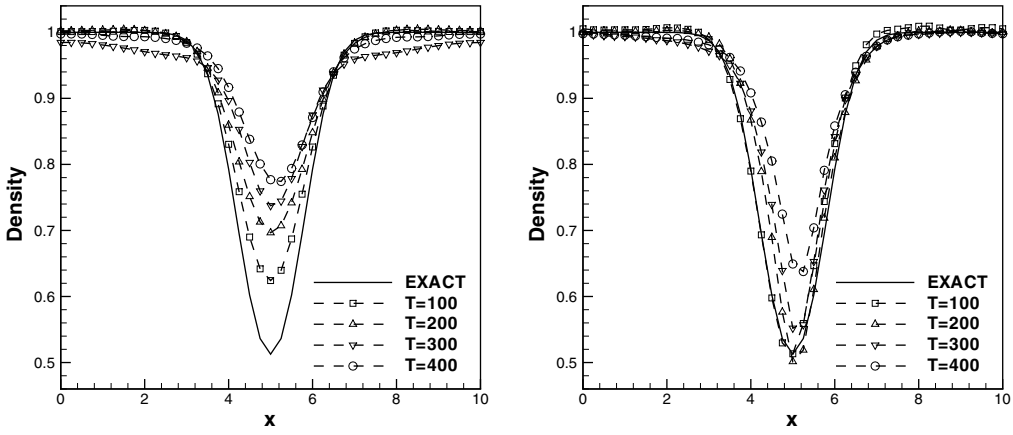

Fig. 11. Density distributions of the convecting vortex along the center line at $t = 100$, 200, 300, and 400 using the WENO5 scheme (left) and the hybrid central-WENO scheme [$r_c = 0.1$] (right) with a 41×40 grid system.

Table 2
Convergence test for the vortex evolution problem

Scheme	Size	L_1 error	L_1 order	L_∞ error	L_∞ order
WENO5	25×25	5.6303E − 2		8.1172E − 1	
	50×50	4.8654E − 3	3.53	8.3836E − 2	3.28
	75×75	9.0182E − 4	4.16	1.7957E − 2	3.80
	100×100	2.4801E − 4	4.49	5.9807E − 3	3.82
Present	25×25	2.2876E − 3		3.4946E − 2	
	50×50	1.6160E − 4	3.82	4.3990E − 3	2.99
	75×75	2.7484E − 5	4.37	8.4351E − 4	4.07
	100×100	8.0167E − 6	4.28	2.2176E − 4	4.64

flow variables is impossible. We can say that the adaptive control of the numerical dissipation in the hybrid central-WENO scheme gives greatly improved resolution compared with the WENO5 scheme and that the resolution power of the FD-type or FV-type WENO schemes can be also enhanced by a similar technique.

3.4. Mixing-layer/shock interaction

This test case is used to assess the shock and fine scale structure capturing capability of schemes in the presence of complicated flow structures [7,8]. The vortices arising from shear layer instability interact with the impinging shock. The initial convective Mach number of a spatially developing mixing layer is 0.6. An oblique shock originates from the upper-left corner and collides with the shear layer near $x = 90$. The shear layer is deflected and interacts with the shock wave reflecting from the lower wall boundary. The inflow condition is given by

$$u = 2.5 + 0.5\tanh(2y). \tag{58}$$

The convective Mach number is defined by

$$M_c = \frac{u_1 - u_2}{c_1 + c_2}, \tag{59}$$

where $u_1 = 3$, $u_2 = 2$, and $c_1 = c_2 = 0.6$ are two free stream velocities, free stream speeds of sound of the upper (subscript "1") and the lower (subscript "2") streams, respectively. The Reynolds number is set to 500 and fluctuations are added to the inflow as

$$v' = \sum_{k=1}^{2} a_k \cos(2\pi kt/T + \phi_k)\mathrm{e}^{(-y^2/b)} \tag{60}$$

with the period $T = \lambda/u_c$, the wavelength $\lambda = 30$, and the convective velocity $u_c = 2.68$. Other constants are given by $b = 10$, $a_1 = 0.05$, $\phi_1 = 0$, $a_2 = 0.05$, and $\phi_2 = \pi/2$. Detailed description about this problem is available in [7]. A reference is calculated using the WENO5 scheme with a 641×161 grid system and all other results are obtained using a 321×81 grid system. The grid systems are uniform in x-direction and are clustered around the center line in y-direction. We compute up to $t = 113.16$ and the CFL number is set to 0.5. Fig. 14 shows the pressure contours. The first and second figures are obtained using the WENO5 scheme with 641×161 and 321×81 grid systems, respectively. r_c was set to 0.2 for the hybrid central-WENO scheme. The third, fourth, and fifth figures show that the shocks around the vortex near $x = 130$ and the eddy shocks around vortices near $x = 175$ and $x = 190$ can be resolved by the hybrid central-WENO scheme more accurately than by the WENO5 scheme. The third and fourth figures are obtained using the hybrid formulation and the filter formulation with the compact scheme for the linear part, respectively. The filter formulation is slightly less dissipative than the hybrid formulation, but the two formulations give nearly the

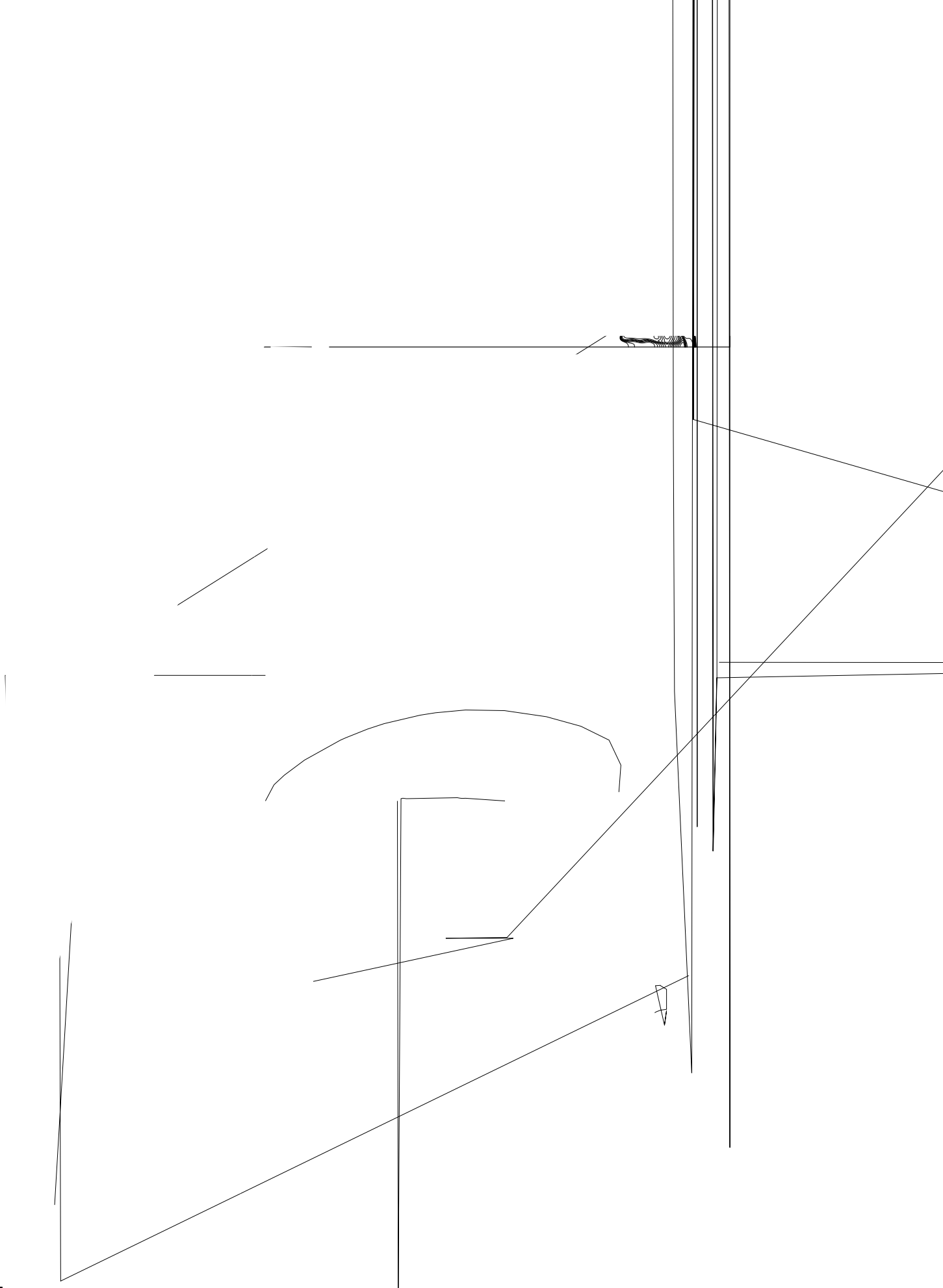

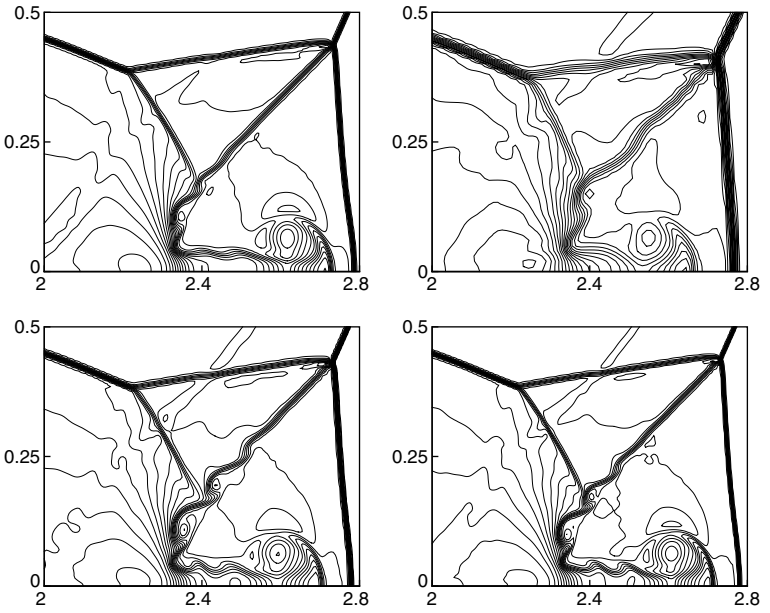

Fig. 13. Close-up view of Fig. 12: the WENO5 scheme (961 × 241) (top left), the hybrid central-WENO scheme (481 × 121) (top right), the hybrid central-WENO scheme (721 × 201) (bottom left), the hybrid central-WENO scheme (961 × 241) (bottom right).

same results. The fifth figure is the result of using the hybrid central-WENO scheme with $r_c = 0.3$. The solution was smeared slightly, but still comparable to that seen in the third and fourth figures. The hybrid central-WENO scheme gives nearly the same resolution as the reference data (the first figure), while the WENO5 scheme smears the flow features slightly.

3.5. Weak shock/vortex interaction

This test case was tailored to investigate the shock-capturing ability of numerical schemes to predict the generation and the transport of acoustic waves during a shock/vortex interaction [16]. The computations are performed on the domain $[0,2] \times [0,2]$. A stationary weak shock is located at $x = 1$, which is prescribed by the pressure jump, $\Delta P/P_\infty = 0.4$, where P_∞ is the static pressure at infinity, corresponding to a reference Mach number $M_0 = 1.1588$. The flow is initialized using the Rankine–Hugoniot relationships. The Reynolds number based on the velocity of the uniform flow is equal to $Re = 2000$. An isolated Taylor vortex is initially superimposed to a uniform flow. The tangential velocity is given by

$$V_\theta(r) = C_1 r \cdot \mathrm{e}^{-C_2 r^2} \tag{61}$$

with

$$C_1 = \frac{U_c}{R_c}\mathrm{e}^{1/2}, \quad C_2 = \frac{1}{2R_c^2}, \quad r = \sqrt{(x-x_0)^2 + (y-y_0)^2}, \tag{62}$$

where $R_c = 0.075$ and $U_c = 0.25$ are used. The initial position of the vortex center is $(x_0,y_0) = (0.5,1)$ and the CFL number is set to 0.5. A reference solution was obtained using the 6th order compact scheme on a very fine uniform 801×501 mesh [16]. Around $t = 0.3$, the vortex meets the standing shock and they interact with each other. Then, acoustic waves are propagated in both directions. In this problem, the vortex shape and the right-moving acoustic wave after interaction are investigated. Fig. 15 shows density distributions

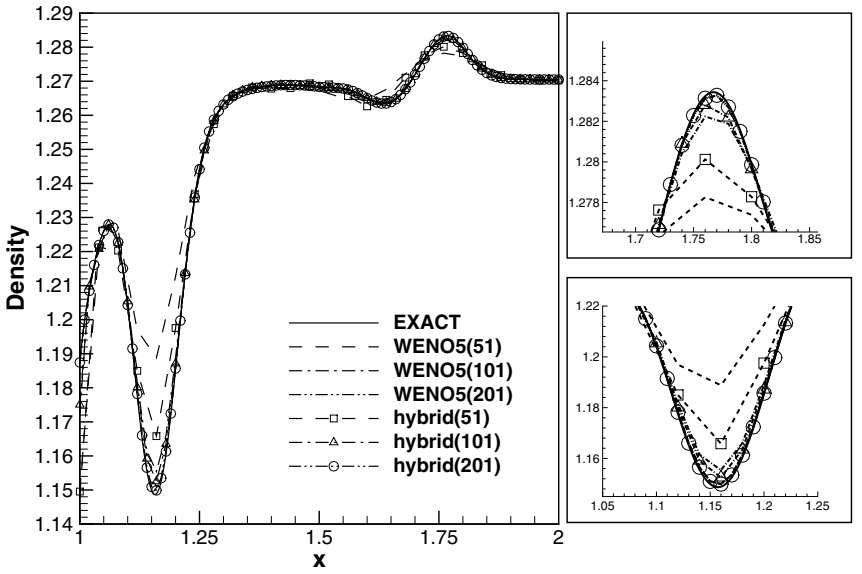

Fig. 15. Density distributions of the weak shock/vortex interaction at $t = 0.7$ along the center line using the WENO5 scheme and the hybrid central-WENO scheme [$r_c = 0.15$] with various grid systems.

along the center line at $t = 0.7$ using 51×51, 101×101, and 201×201 grid systems (the numbers in parentheses, "51", "101", and "201", denote the grid systems used). $r_c = 0.15$ for the hybrid central-WENO scheme was used. For the coarse grid system, 51×51, the hybrid central-WENO scheme gives a much better numerical solution for the post-shock vortex and the right-moving acoustic wave than the WENO5 scheme. As the grid system becomes finer, the numerical solutions from the two schemes approach the reference solution. Fig. 16 shows density distributions using the hybrid central-WENO scheme and the filter

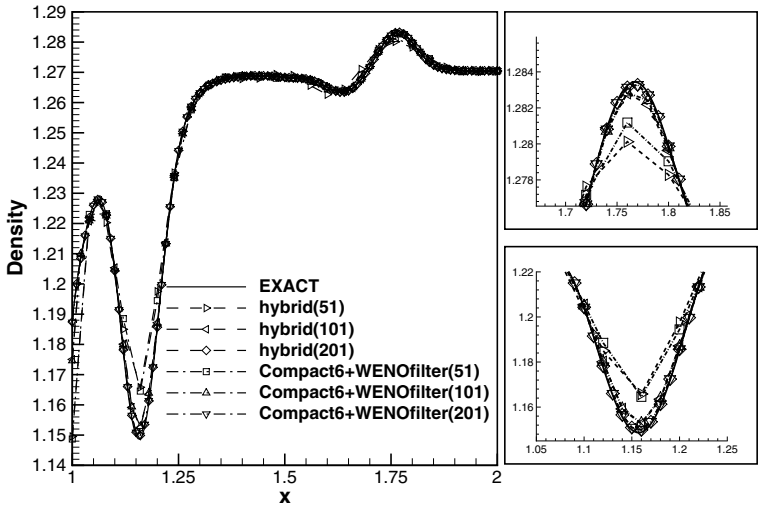

Fig. 16. Density distributions of the weak shock/vortex interaction at $t = 0.7$ along the center line using the hybrid central-WENO scheme and the filter formulation (compact6 + WENO filter) [$r_c = 0.15$] with various grid systems.

formulation with the 6th order compact scheme. $r_c = 0.15$ was used for the two formulations. The filter formulation is slightly more accurate than the hybrid formulation due to the compact scheme for the linear part. Though the figures are not displayed, simulations using the hybrid central-WENO scheme with $r_c = 0.3$ are indistinguishable from those with $r_c = 0.15$.

4. Concluding remarks

A hybrid central-WENO scheme has been proposed. Two sub-schemes, the WENO5 scheme and the central flux scheme, were hybridized by means of a weighting function. The first derivative of flux at the cell center obtained by the derived hybrid central-WENO scheme is expressed as a combination of the 6th order central difference scheme and the numerical dissipation of the WENO5 scheme, which is controlled adaptively. Because of its structure, the proposed hybrid scheme can be considered a filter scheme. We compared the performance of the proposed hybrid central-WENO scheme with those of other hybrid schemes and with that of the WENO5 scheme, and we have shown that our hybrid scheme has great computational efficiency and resolution power. Two formulations, the hybrid and the filter formulations, are also compared in this research. It is found that the filter formulation using the efficient compact scheme can give a slightly improved resolution for rather smooth flows, but it is weak for flows that have strong shocks. A complete switch to the WENO5 scheme guaranteeing monotonicity can not be achieved in regions with strong shocks. Although this type of hybrid scheme has a drawback in that the user determines the threshold value r_c, r_c values around 0.3 have given robust and accurate results for our several numerical experiments with linear and non-linear cases.

References

[1] C.W. Shu, S. Osher, Efficient implementation of essentially non-oscillatory shock capturing schemes II, J. Comput. Phys. 83 (1989) 32–78.
[2] G.S. Jiang, C.W. Shu, Efficient implementation of weighted ENO schemes, J. Comput. Phys. 126 (1996) 202–228.
[3] D.S. Balsara, C.W. Shu, Monotonicity preserving weighted essentially non-oscillatory schemes with increasingly high order of accuracy, J. Comput. Phys. 160 (2000) 405–452.
[4] A.I. Tolstykh, High Accuracy Non-centered Compact Difference Schemes for Fluid Dynamics Applications, World Scientific, Singapore, 1994.
[5] S.K. Lele, Compact finite difference schemes with spectral-like resolution, J. Comput. Phys. 103 (1992) 16–42.
[6] C.K.W. Tam, J.C. Webb, Z. Dong, A study of the short wave components in computational acoustics, J. Comput. Acoust. 1 (1993) 1–30.
[7] H.C. Yee, N.D. Sandham, M.J. Djomehri, Low-dissipative high-order shock-capturing methods using characteristic-based filters, J. Comput. Phys. 150 (1999) 199–238.
[8] H.C. Yee, M. Vinokur, M.J. Djomehri, Entropy splitting and numerical dissipation, J. Comput. Phys. 162 (2000) 33–81.
[9] B. Sjögreen, H.C. Yee, Multiresolution wavelet based adaptive numerical dissipation control for high order methods, J. Sci. Comput. 20 (2004) 211–255.
[10] E. Garnier, P. Sagaut, M. Deville, A class of explicit ENO filters with application to unsteady flows, J. Comput. Phys. 170 (2001) 184–204.
[11] D. Kim, J.H. Kwon, A low dissipative and dispersive scheme with a high order WENO dissipation for unsteady flow analyses, AIAA paper 2004–2705, 2004.
[12] N.A. Adams, K. Shariff, A high-resolution hybrid compact-ENO scheme for shock-turbulence interaction problems, J. Comput. Phys. 127 (1996) 27–51.
[13] S. Pirozzoli, Conservative hybrid compact-WENO schemes for shock-turbulence interaction, J. Comput. Phys. 178 (2002) 81–117.
[14] Y.X. Ren, M. Liu, H. Zhang, A characteristic-wise hybrid compact-WENO scheme for solving hyperbolic conservation laws, J. Comput. Phys. 192 (2003) 365–386.
[15] P. Woodward, P. Colella, The numerical simulation of two-dimensional fluid flow with strong shocks, J. Comput. Phys. 54 (1984) 115–173.

[16] C. Tenaud, E. Garnier, P. Sagaut, Evaluation of some high-order shock capturing schemes for direct numerical simulation of unsteady two-dimensional free flows, Int. J. Numer. Meth. Fluid 33 (2000) 249–278.
[17] V.V. Rusanov, Calculation of interaction of non-steady shock waves with obstacles, USSR J. Comp. Math. Phys. 1 (1961) 267–279.
[18] P. Batten, M.A. Leschziner, U.C. Goldberg, Average-state Jacobian and implicit methods for compressible viscous and turbulent flows, J. Comput. Phys. 137 (1997) 38–78.
[19] X. Deng, M. Mao, High-order dissipative weighted compact nonlinear schemes for Euler and Navier–Stokes equations, AIAA Paper 2001–2626, 2001.
[20] R. Vichnevetsky, J.B. Bowles, Fourier Analysis of Numerical Approximations of Hyperbolic Equations, SIAM, Philadelphia, 1982.
[21] G. Billet, O. Louedin, Adaptive limiters for improving the accuracy of the MUSCL approach for unsteady flows, J. Comput. Phys. 170 (2001) 161–183.
[22] J. Shi, Y.T. Zhang, C.W. Shu, Resolution of high order WENO schemes for complicated flow structures, J. Comput. Phys. 186 (2003) 690–696.